The potential of satellite spectro-imagery for monitoring CO2 emissions from large cities

Grégoire Broquet, Francois-Marie Breon, Emmanuel Renault, Michael Buchwitz, Maximilian Reuter, Heinrich Bovensmann, Frédéric Chevallier, Lin Wu, Philippe Ciais

Atmos. Meas. Tech., 11, 681–708, 2018
https://doi.org/10.5194/amt-11-681-2018

Atmospheric Measurement Techniques
Open Access
EGU

The potential of satellite spectro-imagery for monitoring CO_2 emissions from large cities

Grégoire Broquet[1], François-Marie Bréon[1], Emmanuel Renault[1,a], Michael Buchwitz[2], Maximilian Reuter[2], Heinrich Bovensmann[2], Frédéric Chevallier[1], Lin Wu[1], and Philippe Ciais[1]

[1]Laboratoire des Sciences du Climat et de l'Environnement, LSCE/IPSL, CEA-CNRS-UVSQ, Université Paris-Saclay, 91191 Gif-sur-Yvette, France
[2]Institute of Environmental Physics (IUP), University of Bremen FB1, Otto Hahn Allee 1, 28334 Bremen, Germany
[a]now at: Service hydrographique et océanographique de la marine, 29228 Brest, France

Correspondence: Grégoire Broquet (gregoire.broquet@lsce.ipsl.fr)

Received: 20 March 2017 – Discussion started: 4 August 2017
Revised: 16 December 2017 – Accepted: 2 January 2018 – Published: 7 February 2018

Abstract. This study assesses the potential of 2 to 10 km resolution imagery of CO_2 concentrations retrieved from the shortwave infrared measurements of a space-borne passive spectrometer for monitoring the spatially integrated emissions from the Paris area. Such imagery could be provided by missions similar to CarbonSat, which was studied as a candidate Earth Explorer 8 mission by the European Space Agency (ESA). This assessment is based on observing system simulation experiments (OSSEs) with an atmospheric inversion approach at city scale. The inversion system solves for hourly city CO_2 emissions and natural fluxes, or for these fluxes per main anthropogenic sector or ecosystem, during the 6 h before a given satellite overpass. These 6 h correspond to the period during which emissions produce CO_2 plumes that can be identified on the image from this overpass. The statistical framework of the inversion accounts for the existence of some prior knowledge with 50 % uncertainty on the hourly or sectorial emissions, and with $\sim$25 % uncertainty on the 6 h mean emissions, from an inventory based on energy use and carbon fuel consumption statistics. The link between the hourly or sectorial emissions and the vertically integrated column of CO_2 observed by the satellite is simulated using a coupled flux and atmospheric transport model. This coupled model is built with the information on the spatial and temporal distribution of emissions from the emission inventory produced by the local air-quality agency (Airparif) and a 2 km horizontal resolution atmospheric transport model. Tests are conducted for different realistic simulations of the spatial coverage, resolution, precision and accuracy of the imagery from sun-synchronous polar-orbiting missions, corresponding to the specifications of CarbonSat and Sentinel-5 or extrapolated from these specifications. First, OSSEs are conducted with a rather optimistic configuration in which the inversion system is perfectly informed about the statistics of the limited number of error sources. These OSSEs indicate that the image resolution has to be finer than 4 km to decrease the uncertainty in the 6 h mean emissions by more than 50 %. More complex experiments assess the impact of more realistic error estimates that current inversion methods do not properly account for, in particular, the systematic measurement errors with spatially correlated patterns. These experiments highlight the difficulty to improve current knowledge on CO_2 emissions for urban areas like Paris with CO_2 observations from satellites, and call for more technological innovations in the remote sensing of vertically integrated columns of CO_2 and in the inversion systems that exploit it.

1 Introduction

Measurements of CO_2 atmospheric concentrations have been used for decades to estimate CO_2 natural surface fluxes at global to regional scales based on atmospheric transport modelling and statistical atmospheric inversion techniques (Peylin et al., 2013). There is now a growing political and scientific interest for the atmospheric monitoring of CO_2 emissions from cities (Duren and Miller, 2012). This has encouraged the investigation of space-borne imagery techniques for

CO_2 concentrations at, typically, 2 to 10 km spatial resolution. The idea is that these techniques may have a high potential for characterizing the plumes of CO_2 downwind large cities, which could be used to quantify the underlying emissions based on an atmospheric inversion approach. Examples of satellite CO_2 imagery concepts are (i) the CarbonSat mission which was a candidate for ESA's Earth Explorer 8 opportunity (Bovensmann et al., 2010; Buchwitz et al., 2013; Sierk et al., 2014), (ii) a project to measure CO_2 with the European Sentinel-5 mission for which a preliminary study of feasibility was conducted but which was not retained (Chimot et al., 2012), (iii) a European satellite dedicated to CO_2 anthropogenic emissions that is presently studied by ESA and the European Commission (Ciais et al., 2015) and (iv) the GeoCARB geostationary mission, which has been selected as an Earth Venture Mission by NASA (O'Brien et al., 2016). The first three of these concepts rely on CO_2 imagery from sun-synchronous and low Earth orbit (LEO) satellites based on differential absorption measurements in the shortwave infrared (SWIR). The SWIR instruments presently appear to be the most suitable for the monitoring of CO_2 surface fluxes, because of their sensitivity to CO_2 concentrations in the planetary boundary layer, where the signal of these fluxes is the largest (Buchwitz et al., 2015). The proposed swath width of CarbonSat was on the order of 200–300 km with a $\sim$ 2 km horizontal resolution, whereas that of Sentinel-5 is much larger, i.e. $\sim$ 2000 km with a 7 km horizontal resolution. The swath has a direct impact on the revisit period. These missions cannot sample CO_2 in cloudy areas, but, weather permitting, this revisit period is close to one day for Sentinel-5 and larger than a week for a CarbonSat-like system. These missions should be envisaged as part of constellations (Velazco et al., 2011) and of integrated observation frameworks including in situ networks. However, given the lack of concept regarding the potential synergy between different space missions and in situ networks for monitoring city emissions, there is a need to study the ability of each space mission to bring information on the emissions from individual cities as a stand alone observation system.

There have been attempts to exploit the space-borne measurements of vertically integrated columns of dry air mole fractions of CO_2 (XCO_2) based on SWIR instruments on board SCIAMACHY or GOSAT for the large-scale inverse modelling of CO_2 natural fluxes (Buchwitz et al., 2015; Basu et al., 2013; Chevallier et al., 2014). These previous works demonstrate the large detrimental impacts of atmospheric transport model errors, underlying the inversion systems, and of the so-called systematic errors in the XCO_2 retrievals. Conversely to the radiometric measurement noise, these systematic errors, which are connected to uncertainties in the atmospheric radiative transfer, have coherent spatial patterns consistent with variations in, e.g., surface albedo, atmospheric aerosols or thin clouds (Chevallier, 2015). The first releases of XCO_2 data from SWIR measurements by OCO-2, which was put into orbit during summer 2014, still bear the signature from such systematic errors (Eldering et al., 2017). Subsequently, routine estimates of CO_2 natural fluxes from atmospheric inversion approaches are still based on the assimilation of the sole ground-based in situ measurements (Peylin et al., 2013; Le Quéré et al., 2015).

The application of atmospheric inversions for the monitoring of CO_2 emissions from cities is a recent research activity. Initial results are based on dedicated urban ground-based atmospheric CO_2 measurement networks (Breon et al., 2015; Lauvaux et al., 2013; Turnbull et al., 2015). There has been no attempt at using SCIAMACHY or GOSAT data at this scale due to the low resolution and precision of the SCIAMACHY data or to the scarcity of the sampling by GOSAT. Kort et al. (2012) discussed the possibility to track trends of CO_2 emissions from large cities based on the diagnostics of local enhancements of the GOSAT XCO_2 data over these megacities, Janardanan et al. (2016) also studied local enhancements of the GOSAT XCO_2 over cities. They compared it to CO_2 high-resolution transport simulations and concluded that GOSAT data could be used to detect biases in the inventories of the emissions from large cities. However, none of these studies performed inversions of the city emissions using the GOSAT data.

OCO-2 provides measurements from eight across-track pixels of $\sim$ 1.3 km by $\sim$ 1.3 km resolution. Due to such a high sampling density along the satellite overpass and to their relatively high theoretical precision, OCO-2 data may bring more insight into the XCO_2 field nearby the cities than SCIAMACHY and GOSAT, especially when using the specific targeting mode of this mission (Crisp, 2015). Hakkarainen et al. (2016) highlighted a significant correlation between the spatial anomalies in the OCO-2 data and the spatial distribution of the anthropogenic emissions, and in particular of the large urban areas. Furthermore, Nassar et al. (2017) and Schwandner et al. (2017) derived estimates of CO_2 emissions from large point sources (some large power plants and a volcano) using OCO-2 observations, raising expectations these observations could also be used to estimate the emissions from dense cities. However, the relatively narrow swath of OCO-2 hinders a full view of urban emission plumes. Bovensmann et al. (2010) and Krings et al. (2011, 2016) raised optimism regarding the potential of XCO_2 imagery for the monitoring of point sources such as power plants or cities. Rayner et al. (2014) and O'Brien et al. (2016) assessed the potential of the GeoCARB instrument, which would provide co-located data of vertically integrated columns of dry air mole fractions of both CO_2 and CO (XCO), which is co-emitted with CO_2 by fossil fuel combustion. Their conclusions were less optimistic regarding the potential of the sole imagery of XCO_2, indicating that the XCO imagery should provide a better constraint for the estimate of CO_2 anthropogenic point sources.

The present study aims at analysing the potential of the XCO_2 imagery from a sun-synchronous satellite with a SWIR radiometer like CarbonSat and Sentinel-5 for the mon-

itoring of CO_2 emissions from a megacity. It should also bring some characterization of the potential of the XCO_2 imagery from a geostationary mission like GeoCARB. Efforts are put in place to ensure that this analysis is based on a realistic configuration of the emissions and atmospheric transport in and around an existing megacity, and on realistic estimates of the spatial coverage, of the random noise and of the systematic errors from the XCO_2 imagery. It is based on a state-of-the-art atmospheric inversion methodology, which can be called "pixel-based" since it assimilates the XCO_2 data corresponding to each pixel of the satellite image as independent observations.

The Paris urban area has ~ 11 million people and emits ~ 11–$14\,\mathrm{MtC\,yr^{-1}}$ (Staufer et al., 2016; AIRPARIF, 2013). It covers the administrative city of Paris, which has ~ 2 million people, and its urban surrounding, which has ~ 9 million people. This urban area is chosen as a study case to benefit from the expertise and tools developed for the assimilation of in situ CO_2 measurements from the CO_2-Megaparis and ICOS ground-based networks (Bréon et al., 2015). In particular, the inversions in the present study are based on a "bottom-up" knowledge of the CO_2 emissions at 1 km/1 h resolution from the regional inventory established by the AIPARIF air-quality agency (AIRPARIF, 2013), and on a 2 km resolution configuration of the CHIMERE atmospheric transport model driven by ECMWF meteorological analysis as in Bréon et al. (2015) and Staufer et al. (2016). Furthermore, the Paris urban area is the most populated urban area of Europe and the administrative city of Paris is the densest city of Europe. The emissions from this megacity (mainly from transport and heating) are high and concentrated over a relatively small area. Therefore, it should be a favourable case for the inversion of city emissions based on space-borne imagery. There is no other major city or area of CO_2 emissions in its vicinity, which should help distinguishing the plume of Paris from that of other regional sources. Finally, the topography in the city and in its vicinity is relatively flat and the average wind speed in the region at 100 m above the ground level (m a.g.l.) is $\sim 7\,\mathrm{m\,s^{-1}}$ so that the plume of XCO_2 out of the city should have a relatively simple structure and should be easy to model. By contrast, CO_2 plumes or domes of cities in environment with complex terrain, or affected by sea breezes in coastal areas (Pérez-Landa et al., 2007) are more difficult to simulate. Consequently, the ability to monitor the emissions from the Paris urban area can be seen as a pre-requirement for the more general task of tracking the emissions from other megacities or smaller cities in western Europe.

Preliminary simulations and inversion experiments (using the modelling configuration described in Sect. 2.5) demonstrated that, due to atmospheric diffusion, the signature of the emissions at a given time from the Paris urban area is negligible or hardly detectable in the XCO_2 fields approximately 6 h later. Consequently, an XCO_2 image from a satellite cannot be exploited to infer direct information about the emissions earlier than ~ 6 h before the satellite overpass. Therefore, this study focuses on the analysis of the potential of individual XCO_2 images of the Paris area for inverting the emissions during the 6 h before each satellite overpass, without trying to exploit successive overpasses together. In order to derive statistics that are representative of a wide range of observation conditions, different experiments are conducted for images taken on different days, i.e. with different meteorological conditions, different cloud cover and different occurrences of the satellite systematic errors.

The study focuses on the ability to derive the average emissions from the city over the 6 h periods before the satellite overpasses but also to solve for the temporal variations at hourly resolution during these periods or to solve for the distribution between the main sectors of activity, i.e. traffic, domestic and commercial heating and industrial combustion. This ability to solve for the sectorial distribution is quite equivalent to the ability to solve for some spatial distribution of the emissions since the emissions of each sector of activity have a different spatial distribution.

The potential of the satellite imagery is assessed in terms of improvement of some statistical prior knowledge on the emissions. Using this statistical prior knowledge, some statistical knowledge on XCO_2 derived from the space-borne measurements, and the relationship between the emissions and XCO_2 given by an atmospheric transport model for the Paris area, the atmospheric inversion follows the Bayesian theory to derive a new ("posterior") statistical knowledge on the emissions with lower uncertainties than the prior. The improvement of the knowledge on the emissions enabled by the assimilation of the satellite data is thus quantified in terms of uncertainty reduction.

Since the atmospheric measurement networks are generally sparse, traditional atmospheric inversion applications have used prior knowledge on the CO_2 fluxes to decrease the uncertainties and gaps in the estimate of the fluxes based on the statistical assimilation of the data from these networks. Prior knowledge is generally based on "bottom-up" models or statistical inventories of the processes underlying the fluxes. At city scale, and due to the swath of the satellite imagery, one expects that the inversion may derive good estimates of the emissions using this imagery only, or that such estimates could be used for the independent verification of the "bottom-up" inventories. Even though, strictly speaking, such a purely "top-down" approach is not investigated here, this study can still give insights on the potential for deriving the emissions based on space-borne data only.

The assessment of the uncertainty reduction due to the assimilation of the satellite imagery is based on different observing system simulation experiment (OSSE) configurations, which account for the time, location, spatial resolution and error statistics of the XCO_2 measurements associated with the satellite and instrumental configurations.

Section 2 details the theoretical and practical inversion framework and the principles for the assessment of the poten-

tial of the satellite imagery as a function of its design. Section 3 analyses an "optimistic" assessment of this potential based on a configuration ignoring sources of errors hardly accounted for by state-of-the-art inversion systems, such as biases in the observation operator or observation errors whose spatial correlations have complex patterns. Section 4 diagnoses the impact of such errors. The discussions and conclusions in Sect. 5 address the optimistic and pessimistic assessments in order to infer the robustness and extent of the conclusions that can be derived with state-of-the-art systems regarding the potential of XCO_2 imagery.

2 OSSE framework

The flux uncertainty reduction due to the assimilation of satellite images is defined as the relative difference between the prior and posterior uncertainties in the fluxes. Its statistical characterization is twofold: the statistics of the posterior uncertainties are provided for a given day following the statistical nature of the inversion framework, but they are also sampled for different days, i.e. different atmospheric transport conditions.

For a given day, the atmospheric inversion derives a statistical estimate for a set of n input parameters $\boldsymbol{s} = [s_1 \ldots s_n]^{\mathrm{T}}$ of a linear coupled flux and atmospheric transport model $\boldsymbol{s} \rightarrow \boldsymbol{y} = \mathbf{M}\boldsymbol{s} + \boldsymbol{y}^{\mathrm{fixed}}$ that simulates the satellite image of $XCO_2\,\boldsymbol{y}$. The coupled model is called the observation operator hereafter. This derivation is based on the information brought by the measurements $\boldsymbol{y}^o$. The control parameters underlying the Paris emissions are the target quantities. Other control parameters correspond to sources of uncertainties in the observation operator that can be better handled if explicitly solved for, e.g., the ecosystem fluxes in the region. The other sources of uncertainties and errors affecting the misfits between the model simulations and the measurements that are not controlled by the inversion should be accounted for as errors in the observation space that the inversion attempts at filtering out. In OSSEs, ignoring some of the sources of uncertainties both in the control space and in the observation space yields optimistic results. By controlling the hourly temporal variations or the sectorial distribution of the emissions, the system accounts for the impact of uncertainties in these distributions on the retrieval of 6 h mean emissions before a satellite overpass. Table 1 summarizes the different options taken for the configuration of the OSSEs and Table 2 summarizes the different experiments based on various combinations of these options.

2.1 Spatial domain

The study is based on a regional atmospheric transport configuration with input CO_2 conditions at the boundaries of its domain. The simulation domain is illustrated in Fig. 1. It is approximately centred over the Paris urban area and it encompasses a large part of northern France. This domain is the same as that used in Bréon et al. (2015). It is sufficiently large ($\sim 500\,\mathrm{km} \times 500\,\mathrm{km}$) so that the CO_2 emitted within Paris at a given time does not exit the simulation domain within 6 h, at least with the wind conditions considered in this study. Therefore, in this study, the signature of the emissions from Paris in the XCO_2 field becomes undetectable in the satellite images as a result of the atmospheric transport diffusion or by leaving the swath of a satellite. It does not become undetectable artificially by leaving the simulation domain, which would have biased the evaluation of large-swath satellite configurations.

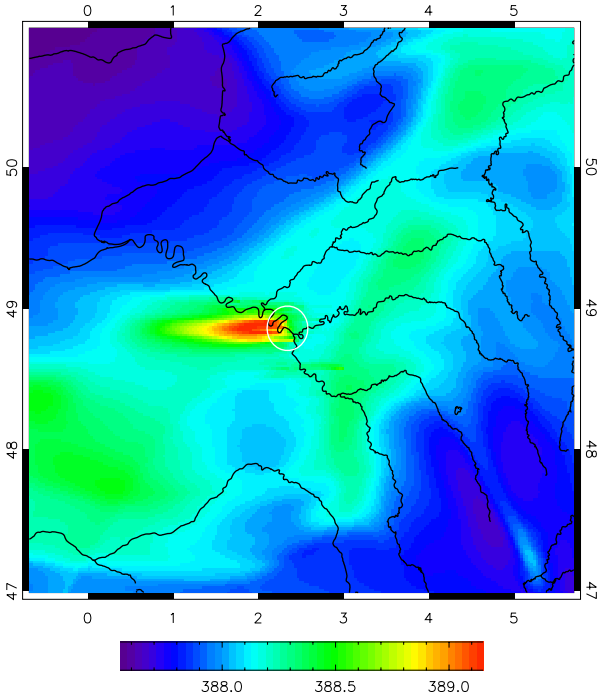

Figure 1. Simulation of XCO_2 (in ppm) over the CHIMERE domain used in this study, on 7 October 2010 at 11:00 and at 2 km resolution using the operator described in Sect. 2.5, the flux budgets given by Airparif and C-TESSEL and the model initial and boundary conditions given by the global LMDZ simulation. The Paris urban area approximately fits within the white circle located at the origin (east) of the plume in the middle of the domain. Most of the emissions of Paris are concentrated close to the centre of the urban area which corresponds to the administrative city of Paris. The longitudes and latitudes of the domain are indicated in degrees east and north.

2.2 Temporal framework

The satellite observation is assumed to occur at 11:00 local time in the morning, in line with the CarbonSat mission requirements (ESA, 2015). In the Paris area, local and UTC time, the latter of which is used hereafter, have a $\sim$9 min 30 s difference, which is negligible. Therefore, the study fo-

Table 1. The different options for the configuration of the OSSEs.

Type of setting	Option	Description
Control vector	Hourly fluxes	$\boldsymbol{s} = \left[\lambda_5^{\mathrm{FF}}, \lambda_6^{\mathrm{FF}}, \lambda_7^{\mathrm{FF}}, \lambda_8^{\mathrm{FF}}, \lambda_9^{\mathrm{FF}}, \lambda_{10}^{\mathrm{FF}}, \lambda_5^{\mathrm{NEE}}, \lambda_6^{\mathrm{NEE}}, \lambda_7^{\mathrm{NEE}}, \lambda_8^{\mathrm{NEE}}, \lambda_9^{\mathrm{NEE}}, \lambda_{10}^{\mathrm{NEE}}, b\right]^{\mathrm{T}}$
	Flux types	$\boldsymbol{s} = \left[\lambda_{\mathrm{Transportation}}^{\mathrm{FF}} \lambda_{\mathrm{Res.\ Combust.}}^{\mathrm{FF}} \lambda_{\mathrm{Comm.\ Combust.}}^{\mathrm{FF}} \lambda_{\mathrm{Large\ Indust.}}^{\mathrm{FF}} \lambda_{\mathrm{Cropland}}^{\mathrm{NEE}}, \lambda_{\mathrm{Grassland}}^{\mathrm{NEE}}, \lambda_{\mathrm{NeedleLeaf\ F.}}^{\mathrm{NEE}}, \lambda_{\mathrm{BroadLeaf\ F.}}^{\mathrm{NEE}}, b\right]^{\mathrm{T}}$
Observation sampling	TH-CarbonSat	Sampling of the 150 km radius circle centred on Paris at 2 km resolution
	TH-LargeSwath	Sampling of the full CHIMERE domain at x km resolution, where $x = 4$, 6, 8 or 10
	SIM-CarbonSat	Sampling from the simulations by Buchwitz et al. (2013) using a 240 km swath
Biases in the observation operator	Emission map	Using $\mathbf{M}_{\mathrm{inventory}} = \mathbf{M}_r^{\mathrm{disc}}$ instead of $\mathbf{M}_{\mathrm{inventory}}^{\mathrm{true}}$ where $r = 15$ or 45 (in km)
	BC	Bias in the Boundary Conditions
Theoretical (system) measurement error	CS	1.1 ppm random noise (1σ)
	Sent5-1 SWIR	2.1 ppm random noise (1σ)
	Sent5-2 SWIR	1.2 ppm random noise (1σ)
	CS space varying	Simulation of random errors by Buchwitz et al. (2013)
	CS incl syst error	Random noise (1σ): root sum square of 0.3 ppm and of the simulation of random errors by Buchwitz et al. (2013)
Practical (actual) measurement error	Theoretical	Consistent with the configuration of the inversion system
	Ensemble	Sampling from the simulation of random errors by Buchwitz et al. (2013)
	Ensemble incl syst error	Sampling from the simulation of random and systematic errors by Buchwitz et al. (2013)
Relevant diagnostic of the posterior uncertainty	Theoretical **A**	Analysis of the posterior uncertainty covariance matrix **A** diagnosed by the inversion system (Eq. 4)
	Theoretical **A** and bias	Analysis of the posterior uncertainty covariance matrix **A** diagnosed by the inversion system (Eq. 4) and of the posterior bias $\boldsymbol{s}^{\mathrm{bias}}$ from Eq. (7)
	Practical **A** and bias	Analysis of the mean and covariance of the sampling of the posterior uncertainty from the Monte Carlo inversion experiments

cuses on the ability to retrieve information on the emissions between 05:00 and 11:00 based on a satellite image acquired at 11:00.

The results are investigated for 20 different days of October 2010, i.e. 20 different transport conditions and 20 different CO_2 domain boundary conditions. These 20 different days encompass a wide range of wind conditions that strongly influence the amplitude, shape and orientation of the XCO_2 plume. They are called hereafter inversion days. In October, the ecosystem fluxes are rather weak, which, in principle, should facilitate the separation between the atmospheric signatures of the natural fluxes and anthropogenic emissions and thus the estimate of the anthropogenic emissions from the XCO_2 imagery.

2.3 Observation space $\boldsymbol{y}$

In the following, we consider instruments with a very good point spread function, so that their measurements are representative of their horizontal sampling, and so that this horizontal sampling is fully characterized by the spatial resolution. The expression "centred on Paris" is used to indicate that an area is centred on the centre of Paris.

ESA (2015) presents two concepts for CarbonSat with 240 and 185 km swaths, and identifies 240 km as a breakthrough requirement for the swath of the mission. Since it accounts for the design of the CarbonSat and Sentinel-5 missions, this study investigates three types of XCO_2 spatial sampling in the Paris area (see Table 1).

The "TH-CarbonSat" sampling (see Fig. S1 in the Supplement) is a full sampling of a 150 km radius circle centred on Paris at 2 km resolution that ignores cloud cover. This theoretical sampling corresponds to an optimistic configuration of the CarbonSat mission with a 300 km swath and to an optimal satellite trajectory for the monitoring of the emissions of Paris. This sampling will be used for optimistic experiments only.

The "TH-LargeSwath" sampling (see Fig. S1) is a full sampling of the whole simulation domain at 4, 6, 8 or 10 km resolution, which ignores cloud cover. This theoretical sampling simulates the acquisition by an instrument with a larger

Table 2. The different OSSEs conducted in the study and their configuration, sorting the group of experiments from the most optimistic to the less optimistic ones.

Name	Control vector	Observation sampling	Biases in the observation operator	Theoretical (system) measurement error	Practical (actual) measurement error	Relevant diagnostic of the posterior uncertainty
TH-2	Hourly fluxes	TH-CarbonSat	None	CS	Theoretical	Theoretical **A**
TH-x-ns*	Hourly fluxes	TH-LargeSwath at x km res	None	Sent5-ns SWIR	Theoretical	Theoretical **A**
THsect-2	Flux types	TH-CarbonSat	None	CS	Theoretical	Theoretical **A**
THsect-x-ns*	Flux types	TH-LargeSwath at x km res	None	Sent5-ns SWIR	Theoretical	Theoretical **A**
Bdist-2-r*	Hourly fluxes	TH-CarbonSat	Emission map: $\mathbf{M}_r^{\text{disc}}$	CS	Theoretical	Theoretical **A** and bias
Bdist-x-ns-r*	Hourly fluxes	TH-LargeSwath at x km res	Emission map: $\mathbf{M}_r^{\text{disc}}$	Sent5-ns SWIR	Theoretical	Theoretical **A** and bias
Bbc-2	Hourly fluxes	TH-CarbonSat	BC	CS	Theoretical	Theoretical **A** and bias
Bbc-x-ns*	Hourly fluxes	TH-LargeSwath at x km res	BC	Sent5-ns SWIR	Theoretical	Theoretical **A** and bias
MC-2	Hourly fluxes	SIM-CarbonSat	None	CS space varying	Ensemble	Practical **A** and bias
MCsyst-2	Hourly fluxes	SIM-CarbonSat	None	CS incl syst error	Ensemble incl syst error	Practical **A** and bias
ALL-2	Hourly fluxes	SIM-CarbonSat	Emission map: $\mathbf{M}_{45}^{\text{disc}}$ and BC	CS incl syst error	Ensemble incl syst error	Practical **A** and bias

* Rows associated with ensembles of experiments with x designating 4, 6, 8 or 10; ns = 1 or 2 and $r = 15$ or 45. Other notations are defined by Table 1.

swath but a smaller spatial resolution than CarbonSat, such as the 7 km resolution instrument on board Sentinel 5. This sampling will also be used for optimistic experiments only.

The "SIM-CarbonSat" samplings (see Figs. S2 and S3) correspond to realistic simulations of the sampling of the Paris area by a 240 km swath instrument with 2 km resolution such as CarbonSat accounting for cloud cover. They are extracted from simulations of CarbonSat sampling over the whole globe and for a full year by Bucwitz et al. (2013). Pillai et al. (2016) also used these simulations to model CarbonSat observations with 240 and 500 km swaths. From these simulations, 69 CarbonSat passes in our modelling domain over the year provide at least 1 XCO_2 data in the 100 km radius circle centred on Paris and are considered to be "over the Paris area". Nineteen different cases are selected from these 69 passes for each of the 20 inversion days in October 2010. These are the 19 simulated passes over the Paris area that provide the best constraints on the emission inversion. This ranking follows the theoretical uncertainty reductions associated with the assimilation of the different sets of observations from the passes as detailed in Sects. 2.8.3 and 4.2. It depends on the number of 2 km × 2 km observations and on their position relative to the emission atmospheric plume, i.e. on the cloud cover and the swath position with respect to the Paris target associated with a pass over the Paris area. Section 4.2 will show that for any inversion day in October, and thus for any of the modelled emission plumes, the constraint on the emission inversion of the 20th best-simulated pass is rather weak. This explains why only 19 simulated passes are selected. The "SIM-CarbonSat" samplings will be used in the less optimistic experiments only. By construction, the CarbonSat acquisitions that are tested for a given inversion day in October 2010 were simulated for other days of the year 2010 by Buchwitz et al. (2013). This is not identified as a significant issue, even though the atmospheric transport conditions of the inversion days could have some inconsistencies with the cloud cover underlying the simulation of these CarbonSat acquisitions.

2.4 Control vector *s*

Hereafter, the CO_2 emissions from anthropogenic activities in the Paris area are denoted: fossil fuel (FF) fluxes, whereas the natural fluxes in the simulation domain are identified as net ecosystem exchange (NEE). The OSSEs investigate the ability of the satellite imagery to solve either for the hourly variations or for the sectorial distribution of the 6 h emissions, and the uncertainties in the estimates of 6 h mean emissions due to uncertainties in either these temporal or sectorial distributions. Two configurations of the control vector are thus used for a given day: either a control vector solving for the hourly fluxes and the background concentration (see its definition below) with 13 parameters (6 for both hourly FF fluxes and hourly NEE and 1 for the background concentration),

$$\boldsymbol{s} = \left[\lambda_5^{\mathrm{FF}}, \lambda_6^{\mathrm{FF}}, \ldots, \lambda_{10}^{\mathrm{FF}}, \lambda_5^{\mathrm{NEE}}, \lambda_6^{\mathrm{NEE}}, \ldots, \lambda_{10}^{\mathrm{NEE}}, b\right]^{\mathrm{T}}, \quad (1)$$

or a control vector solving for the 6 h budgets of the FF CO_2 emissions from transportation, residential combustion, commercial combustion and industrial combustion, and for the distribution of the 6 h budgets of NEE per main plant functional type (PFT: broadleaf forest, needle leaf forests, grasslands, croplands) with 9 parameters (4 for both the sectorial budgets of FF fluxes and the budgets of NEE per land cover type, and 1 for the background concentration):

$$\begin{aligned}\boldsymbol{s} = \big[&\lambda_{\text{Transportation}}^{\mathrm{FF}}, \lambda_{\text{Res. Combust.}}^{\mathrm{FF}}, \lambda_{\text{Comm. Combust.}}^{\mathrm{FF}},\\ &\lambda_{\text{Large Indust.}}^{\mathrm{FF}}, \lambda_{\text{Cropland}}^{\mathrm{NEE}}, \lambda_{\text{Grassland}}^{\mathrm{NEE}}, \lambda_{\text{NeedleLeaf F.}}^{\mathrm{NEE}},\\ &\lambda_{\text{BroadLeaf F.}}^{\mathrm{NEE}}, b\big]^{\mathrm{T}}\end{aligned} \quad (2)$$

In these formal definitions of the control vector, $\lambda_{\mathrm{hh}}^{X}$ (first case) or λ_{Y}^{X} (second case) is a scaling factor for the total flux X (NEE or FF) between time hh and hh + 1 h (first case) or for sector/PFT Y between 05:00 and 11:00 (second case). Almost all of the Paris emissions are distributed among the four FF emission sectors considered in the second configuration of the control vector (see Sect. 2.5.1). With both configurations, controlling scaling factors is equivalent to controlling the budget of the corresponding flux components. In practice, these control parameters are used to rescale the 1 h and 2 km resolution FF and NEE fields corresponding to these components from the Airparif inventory and an ecosystem model (see below the description of the observation operator in Sect. 2.5). The emission maps and the hourly budgets from the Airparif inventory vary in time at the hourly scale (see Sect. 2.5.1). Therefore, if the inversion derives identical scaling factors for different hours, it would not lead to identical estimates of the emission budgets for these different hours. However, the variations of the hourly budgets from the Airparif inventory are sufficiently small to be ignored when comparing uncertainties in scaling factors for different hours in the following. b is the average XCO_2 concentration in the simulation domain at the time of the satellite observation (11:00) due to the very large-scale influence of CO_2 fluxes outside the domain or before 05:00. Its inclusion in the control vector provides a simple account for uncertainties in these remote fluxes. It is thus called "background XCO_2" throughout the text. The general notation $\boldsymbol{s} = [\boldsymbol{\lambda}, b]^{\mathrm{T}}$ is used for both control vectors.

The analysis mainly focuses on results obtained for the control variables related to the Paris emissions which are the target quantities. The control of the NEE could also bring some insights about the inversion of the natural fluxes using satellite data, but this topic is out of the scope of this paper and the experimental framework is not optimized for such analysis.

2.5 The observation operator

The linear observation operator $\boldsymbol{s} \rightarrow \boldsymbol{y} = \mathbf{M}\boldsymbol{s} + \boldsymbol{y}^{\mathrm{fixed}}$ combines three linear operators.

2.5.1 Spatial and temporal distribution of the fluxes

The first operator is the rescaling of 2 km and 1 h resolution fields of emissions from Paris and northern France NEE to generate the fields of total fluxes $\boldsymbol{f}$ in the domain: $\boldsymbol{\lambda} \rightarrow \boldsymbol{f} = \mathbf{M}_{\mathrm{inventory}}\boldsymbol{\lambda}$. The emission and NEE fields are based on estimates from the Airparif inventory for the year 2008 and from simulations with the C-TESSEL vegetation carbon flux model at ECMWF (Boussetta et al., 2013). In order to fully describe the total fluxes in the domain, one must also account for the anthropogenic emissions outside the Paris area that are not covered by the Airparif inventory. However, the OSSEs ignore uncertainties in these emissions (see the corresponding discussion in Sect. 2.9). In practice, since the equations in the OSSEs only solve for the propagation of uncertainties, this is equivalent to ignoring the emissions themselves. Therefore, we do not include these emissions in the observation operator and thus in the simulations used to illustrate the inversion problem in Figs. 1, S1 and S3.

Bréon et al. (2015) also used the Airparif inventory for the year 2008 and the C-TESSEL NEE simulations in their inversion framework. They provided some description and analysis of these products, which are not reminded here. For each inversion day in October 2010, we use the estimates from Airparif for the corresponding day in October 2008 and that from C-TESSEL for the same day in October 2010. The inconsistency between the year of emission estimates and that of the transport simulation is not an issue for the OSSEs.

The resolution of the Airparif inventory is 1 km in space and 1 h in time, and the C-TESSEL NEE is provided at approximately 15 km and 3 h resolution. These products are aggregated or interpolated at 2 km and 1 h resolution, which is the input resolution of the transport model. The sectorial resolution of the Airparif inventory is much more detailed than that considered with the second configuration of the con-

trol vector, which rescales only four main aggregated sectors, representing together more than 95 % of the total emissions. When using this second type of control vector, the NEE from C-TESSEL is interpolated and then disaggregated in each 2 km × 2 km grid cell between the PFT components of the control vector. Since we do not have access to estimates of the NEE per PFT by C-TESSEL, this disaggregation is based on the fractional coverage of each PFT per grid cell, derived from the land cover distribution of the Global Land Cover Facility (GLCF) 1 km × 1 km resolution database from the University of Maryland (Hansen and Reed, 2000).

2.5.2 Atmospheric transport

The second operator is the atmospheric transport of CO_2 in the study domain that yields the temporal and 3-D spatial distribution of CO_2 atmospheric mole fractions $\boldsymbol{c}$: $\boldsymbol{f} \rightarrow \boldsymbol{c} = \mathbf{M}_{\text{transport}}\boldsymbol{f} + \boldsymbol{c}^{\text{bound}}$. This operator is based on the CHIMERE atmospheric transport model (Menut et al., 2013). The term $\boldsymbol{c}^{\text{bound}}$ contains the signature of the domain boundary and initial (at 05:00) CO_2 conditions, called hereafter "boundary conditions". $\boldsymbol{c}^{\text{bound}}$ is decomposed into $b[1, 1\ldots1]^{\text{T}}_{n_c}$ and $\boldsymbol{c}^{\text{fixed}}$, where $[1, 1\ldots1]_{n_c}$ has the length n_c corresponding to the 1-D representation of the 3-D CO_2 concentrations space, $\boldsymbol{c}^{\text{fixed}}$ is not controlled by the inversion, and the vertical (see Sect. 2.5.3) and horizontal integration of $\boldsymbol{c}^{\text{fixed}}$ within the simulation domain at 11:00 is null, so that the vertical and horizontal integration of $\boldsymbol{c}^{\text{bound}}$ at 11:00 yields b.

The CHIMERE configuration used in this study is similar to that used in Bréon et al. (2015); for example, it has the same vertical discretization with 19 vertical levels from the surface up to 500 hPa (P_{top}) and the same physical parameters. It has a 2 km horizontal resolution over the whole simulation domain. ECMWF operational analyses at nearly 15 km resolution are used to provide the meteorological forcing to CHIMERE. This meteorological forcing does not account for urban land surface influences. The impact of urban land surface parameters may be large on the simulation of in situ CO_2 data within or close to the city (Bréon et al., 2015). However, it may be less critical when considering the XCO_2 plumes downwind the city. Furthermore, the objective here is to produce a realistic rather than a precise simulation of the XCO_2 plumes from Paris. Therefore, we may neglect these parameters for our OSSEs.

The CO_2 mixing ratios at the lateral and top boundaries of the CHIMERE model and the initial conditions at 05:00 (i.e. $\boldsymbol{c}^{\text{fixed}}$) are imposed using outputs from a global LMDZ simulation at 3.75° (longitude) × 2.5° (latitude) resolution assimilating in situ CO_2 data from a global ground-based measurement network (Chevallier et al., 2010).

2.5.3 Vertical integration of the CO_2 column

The third operator is the computation of XCO_2 data $\boldsymbol{y}$ for a given satellite observation sampling based on the 3-D CO_2 concentrations at 11:00 in the CHIMERE domain, from the surface up to P_{top}: $\boldsymbol{c} \longrightarrow \boldsymbol{y} = \mathbf{M}_{\text{integ}}\boldsymbol{c}$. Part of this computation includes the aggregation of the 2 km horizontal resolution CO_2 fields at the chosen satellite image resolution. For the sake of simplicity and since we use synthetic data only, it is assumed that the satellite observation has a uniform vertical weighting function for each horizontal pixel of a given satellite space sampling (see above Sect. 2.3). For a given horizontal pixel at latitude "lat" and longitude "lon", XCO_2 is thus computed from the average of the vertically distributed CO_2 mole fractions:

$$\mathrm{XCO_2}(\text{lon},\ \text{lat}) = \frac{1}{P_{\text{surf}}(\text{lon},\ \text{lat})} \left(\int_{P_{\text{top}}}^{P_{\text{surf}}(\text{lon},\ \text{lat})} \mathrm{CO_2}(\text{lon},\ \text{lat},\ p)\mathrm{d}p + \overline{\mathrm{CO_2}}(P_{\text{top}})\,P_{\text{top}} \right), \quad (3)$$

where p is the pressure and P_{surf} is the surface pressure. In this equation, a uniform concentration equal to the horizontal average of the top level mixing ratios in CHIMERE: $\overline{\mathrm{CO_2}}\left(P_{\text{top}}\right)$ is assumed to apply at all pressures lower than P_{top}. This simple approximation is used since the surface fluxes in the simulation domain do not impact the concentration close to the top of the model within the simulation time. It ignores the signature of remote fluxes above 500 hPa and we implicitly assume that this signature will not significantly impact the inversion of the emissions from the Paris area. This equation also ignores the slant path of the columns that would be measured by a satellite within the model. Finally it ignores the potential impact of the water vapour content of the atmosphere on the vertical weighting function of the satellite measurements.

2.5.4 Practical computation of the observation operator

The observation operator $\boldsymbol{s} \rightarrow \boldsymbol{y} = \mathbf{M}\boldsymbol{s} + \boldsymbol{y}^{\text{fixed}}$ can be rewritten $\boldsymbol{s} \rightarrow \boldsymbol{y} = \mathbf{M}_{\text{integ}}\mathbf{M}_{\text{transport}}\mathbf{M}_{\text{inventory}}\boldsymbol{\lambda} + b[1, 1\ldots1]^{\text{T}}_{n_y} + \boldsymbol{y}^{\text{fixed}}$, where $[1, 1\ldots1]_{n_y}$ has the length n_y corresponding to the 1-D representation of the observation space. In order to apply the inversion equations analytically (see Sect. 2.6 below), the $\mathbf{M}$ matrix is built explicitly. For this, the $\mathbf{M}_{\text{integ}}\mathbf{M}_{\text{transport}}\mathbf{M}_{\text{inventory}}$ matrix is built by computing each of its column $\boldsymbol{m}_j$ through the application of the operator $\boldsymbol{\lambda} \rightarrow \boldsymbol{y} = \mathbf{M}_{\text{integ}}\mathbf{M}_{\text{transport}}\mathbf{M}_{\text{inventory}}\boldsymbol{\lambda}$ to unit vectors $\boldsymbol{\lambda}_j = [0\ldots0\,1\,0\ldots0]^{\text{T}}$, where only the jth control parameter corresponding to a flux scaling factor is set to 1 and others are set to 0. The small number of control parameters makes the number of simulations $\boldsymbol{\lambda}_j \rightarrow \boldsymbol{m}_j = \mathbf{M}_{\text{integ}}\mathbf{M}_{\text{transport}}\mathbf{M}_{\text{inventory}}\boldsymbol{\lambda}_j$ computationally affordable. The columns $\boldsymbol{m}_j$ correspond to the response functions in terms of XCO_2 to each of the Airparif or C-TESSEL flux component controlled by a scaling factor (see an illustration of these response functions in Fig. S4).

The full observation operator matrix $\mathbf{M}$ is obtained by adding the column $[1, 1 \ldots 1]^{\mathrm{T}}_{n_y}$ to $\mathbf{M}_{\mathrm{integ}}\mathbf{M}_{\mathrm{transport}}\mathbf{M}_{\mathrm{inventory}}$ which corresponds to the homogeneous distribution in space of b, the background XCO_2 at 11:00.

2.6 Theoretical framework of the atmospheric inversion

The theoretical framework of the inversion system used here in the OSSEs is the one traditionally used for atmospheric inversions. It is based on the Bayesian update of a statistical prior estimate of the control vector $\boldsymbol{s}$, using statistical information from the assimilation of the measurements $\boldsymbol{y}^o$ in the observation operator. The usual assumption is that the prior estimate has a Gaussian distribution $N(\boldsymbol{s}^b, \mathbf{B})$ and that the distribution of the misfits between the simulated observations $\mathbf{M}\boldsymbol{s} + \boldsymbol{y}^{\mathrm{fixed}}$ and $\boldsymbol{y}^o$ that are not due to errors in $\boldsymbol{s}$ (i.e. the so-called observation errors, which include atmospheric transport and representation errors) is unbiased, has a Gaussian distribution $N(\mathbf{0}, \mathbf{R})$, and is not correlated with the prior uncertainty. In that case, the Bayesian update of the estimate of $\boldsymbol{s}$, called hereafter the posterior distribution, is a Gaussian distribution $N(\boldsymbol{s}^{\mathrm{a}}, \mathbf{A})$, with $\boldsymbol{s}^{\mathrm{a}}$ being the best estimate of the actual $\boldsymbol{s}$ knowing $\boldsymbol{s}^b$ and $\boldsymbol{y}^o$, and $\mathbf{A}$ characterizing the uncertainty in this estimate. The problem simplifies into deriving (Tarantola, 2005):

$$\mathbf{A} = \left[\mathbf{B}^{-1} + \mathbf{M}^{\mathrm{T}}\mathbf{R}^{-1}\mathbf{M}\right]^{-1} \tag{4}$$

and

$$\boldsymbol{s}^a = \boldsymbol{s}^b + \mathbf{K}\left(\boldsymbol{y}^o - \mathbf{M}\boldsymbol{s}^b - \boldsymbol{y}^{\mathrm{fixed}}\right) \tag{5}$$

by denoting

$$\mathbf{K} = \mathbf{A}\mathbf{M}^{\mathrm{T}}\mathbf{R}^{-1}. \tag{6}$$

The inversion system solves for these equations analytically based on the explicit computation of all matrices and vectors.

Hereafter, we characterize the uncertainties by their standard deviations and correlations. The scores of "uncertainty" and "uncertainty reductions" that we give for a given scalar quantity, a single flux budget or parameter refer to the standard deviation of the uncertainties σ in this scalar quantity, and to the relative difference between its prior and posterior values: $1 - \sigma_a/\sigma_b$. An exception occurs when explicitly accounting for biases (see Sect. 2.8.2 and 2.8.3 below), in which case the scores of "uncertainty" and "uncertainty reductions" refer to the root mean square (RMS) values of the uncertainties and to the relative difference between these prior and posterior RMS values.

2.7 Prior uncertainty

In all cases, our framework assumes that the prior uncertainty in individual scaling factors for the fluxes, i.e. the relative uncertainty in the budget of the corresponding flux components from the observation operator is 50 %; that there is no correlation between uncertainties in the different scaling factors; and that the uncertainty in b is 10 ppm. $\mathbf{B}$ can thus be written $\mathbf{B} = \mathrm{diag}([0.5^2, 0.5^2 \ldots 0.5^2, 10^2\ \mathrm{ppm}^2]^{\mathrm{T}})$ denoting hereafter $\mathrm{diag}(\boldsymbol{v})$ for a diagonal matrix whose diagonal is defined by the terms in vector $\boldsymbol{v}$. This results in a small inconsistency regarding the uncertainty in the total 6 h mean emissions from Paris when controlling the hourly fluxes or the fluxes for the different sectors of activity: it is nearly equal to 22.4 or 26 % respectively, even though it also slightly depends on the days. Such a difference depending on the control vector also applies to the 6 h mean NEE. These differences are negligible in the framework of the OSSEs considered here. The sensitivity of the results to the control vector configuration is mainly indicative of the impact of uncertainties in the temporal profile vs. the sectorial distribution of the emissions, and not of the impact of changes of the prior uncertainty in the 6 h mean emissions.

2.8 Observation errors and practical implementation of the OSSEs

Tables 1 and 2 summarize the different configurations of the OSSEs. Different types of OSSEs are conducted with different levels of agreement between the statistics of the synthetic observation errors that are introduced in practice and the assumptions underlying the theoretical framework of the inversion system.

2.8.1 Analytical computation of the posterior uncertainties when considering only a measurement noise that is perfectly accounted for by the inversion system

In the first set of OSSEs, errors from the observation operator are ignored and the observation errors are limited to a Gaussian noise in the measurements. The standard deviation of this noise is perfectly consistent with the configuration of the $\mathbf{R}$ matrix in the inversion system. In this case, the assumptions made through the set-up of the inversion system are exact, and the matrix $\mathbf{A}$ obtained from the application of Eq. (4) is a perfect estimate of the uncertainties in the inverted fluxes. $\mathbf{A}$ and its comparison to $\mathbf{B}$, i.e. the analysis of the so-called uncertainty reduction due to the assimilation of the measurements, are the proper indicators of the satellite data potential. Since $\mathbf{A}$ depends on $\mathbf{B}$, $\mathbf{R}$ and $\mathbf{M}$ only, the building of synthetic data is unnecessary. The corresponding OSSEs will use the two first types of satellite spatial sampling described in Sect. 2.3 only (TH-CarbonSat and TH-LargeSwath). A uniform value that does not vary in space or time for a given satellite configuration is used for the standard deviation of the measurement noise. This ignores the issue that, in principle, the standard deviation of the measurement noise should vary significantly with the solar zenith angle, the surface albedo and the atmospheric content. For TH-CarbonSat sampling,

this uniform value is derived as a typical value from the simulations of CarbonSat random errors over the Paris area performed by Buchwitz et al. (2013). For the TH-LargeSwath sampling, the values are derived from the ESA Sentinel 5 study (Chimot et al., 2012) with two options corresponding to hypothetical instruments with one or two SWIR bands: the 2.0 µm and optionally the 1.6 µm absorption bands. $\mathbf{R}$ is thus set up as $(e^r)^2\mathbf{I}_d$, where e^r ranges from 1.1 to 2.1 ppm depending on the satellite configuration (see Table 1) and $\mathbf{I}_d$ is the identity matrix in the observation space.

All inversions solving for the fluxes per sector of activity and per PFT will be conducted with this OSSE framework and with these assumptions regarding the observation errors. The other types of OSSEs and assumptions on the observations errors will be tested with the inversion of hourly emissions only. This choice is based on the analysis of the first set of OSSEs discussed in Sect. 3.2 and 3.3.

2.8.2 Analytical computation of the impact of biases from the observation operator

In the second set of OSSEs, biases $\boldsymbol{y}^{\text{bias}}$ from the observation operator and thus in the observation errors are introduced in addition to the measurement noise. They impact the difference $\boldsymbol{y}^0 - \mathbf{M}\boldsymbol{s}^b - \boldsymbol{y}^{\text{fixed}}$. Such biases cannot be accounted for by the theoretical framework of the inversion systems and generate a bias in the posterior estimate of the control vector equal to

$$\boldsymbol{s}^{\text{bias}} = \mathbf{K}\boldsymbol{y}^{\text{bias}}. \tag{7}$$

This bias will be computed along with $\mathbf{A}$ and both this bias and $\mathbf{A}$ will have to be compared to $\mathbf{B}$ in order to infer the potential of the satellite data assimilation. The second set of OSSEs will use the two first types of satellite spatial sampling only (TH-CarbonSat and TH-LargeSwath) and the value for $\mathbf{R} = (e^r)^2\mathbf{I}_d$ as defined above for the first set of OSSEs.

Two types of biases in the observation operator will be investigated. The first type of bias is related to the spatial distribution of the emissions of Paris. The operator $\mathbf{M}_{\text{inventory}}$ used by the inversion system could strongly differ from the actual distribution of the emissions $\mathbf{M}^{\text{true}}_{\text{inventory}}$. Assuming that this difference is a bias and not a random error, which makes sense given the relatively weak temporal variability of the spatial distribution of the emissions, one can easily demonstrate that this generates a bias in the estimate of the true control vector $\boldsymbol{s}^{\text{true}}$, which is given by

$$\boldsymbol{s}^{\text{bias}} = \mathbf{K}\left(\mathbf{M}^{\text{true}}_{\text{inventory}} - \mathbf{M}_{\text{inventory}}\right)\boldsymbol{s}^{\text{true}}. \tag{8}$$

This does not yield any additional random posterior uncertainty compared to that characterized by the $\mathbf{A}$ covariance matrix derived from Eq. (4). We thus associate it with a bias in the observation errors:

$$\boldsymbol{y}^{\text{bias}} = \left(\mathbf{M}^{\text{true}}_{\text{inventory}} - \mathbf{M}_{\text{inventory}}\right)\boldsymbol{s}^{\text{true}}. \tag{9}$$

In an extreme case where the spatial distribution of the emissions in the Paris area is fully ignored, one could distribute the emissions homogeneously over a disc whose radius would be approximately that of the Paris urban cover. The difference between the homogeneous distribution over a disc and the distribution from Airparif is used here to simulate a bias in an observation operator that would be built on rough information about the urban extent only.

For the OSSEs investigating the impact of such a bias in the emission spatial distribution, two new observation operators have been computed by replacing the spatial distribution of the Paris emissions from Airparif by a homogeneous one over two different discs centred on Paris with 15 and 45 km radius respectively (denoting $\mathbf{M}_{\text{inventory}} = \mathbf{M}^{\text{disc}}_{15}$ and $\mathbf{M}^{\text{disc}}_{45}$ respectively), but keeping the same hourly emission budgets as in Airparif. These two radiuses are defined so that the first disc is smaller than the Paris urban area, while the second one encompasses all this area. The bias is computed with $\boldsymbol{s}^{\text{true}} = \left[\boldsymbol{\lambda}^{\text{true}}, b^{\text{LMDZ}}\right]^{\text{T}}$, where b^{LMDZ} is set according to the average of the LMDZ simulation used to generate $\boldsymbol{c}^{\text{fixed}}$ (see Sect. 2.5.2) and where $\boldsymbol{\lambda}^{\text{true}} = [1, 1 \ldots 1]^{\text{T}}_{n_\lambda}$, i.e. assuming that the LMDZ provides the true background XCO_2 and that Airparif has the true estimates of the hourly total emissions. This is relevant since this second type of OSSEs aims at deriving a qualitative assessment rather than a precise quantification of the impact of biases in the observation operator.

Of note is the fact that this modification of the observation operator impacts, in practice, Eq. (4) and thus the theoretical posterior uncertainties. The $\mathbf{A}$ matrices obtained with $\mathbf{M}^{\text{disc}}_{15}$ and $\mathbf{M}^{\text{disc}}_{45}$ differ from that obtained with $\mathbf{M}_{\text{inventory}}$ in the first set of OSSEs, which relied on a perfect knowledge of the spatial distribution of the emissions. It is thus critical to analyse this change of the random posterior uncertainty.

The second type of bias in the observation operator investigated in this study is connected to errors in the estimate of the CO_2 boundary conditions, i.e. in the term $\boldsymbol{y}^{\text{fixed}} = \mathbf{M}_{\text{integ}}\boldsymbol{c}^{\text{fixed}}$ defined in Sect. 2.5. The uncertainty in the boundary conditions would be traditionally considered as random in the usual mathematical framework of the inversions. Here, the average impact of the boundary conditions is implicitly assumed to bear random errors through the control of the background concentrations b and the definition of their prior uncertainties. However, the boundary conditions from a very large-scale simulation that misses the right structure of CO_2 transported from large and heterogeneous sources and sinks close to the boundaries, e.g. the anthropogenic emissions in Belgium and in the Netherlands, can bear biases. Tests are conducted by assuming that the bias in $\boldsymbol{c}^{\text{fixed}}$ is given by the transport with CHIMERE of the variations in space and time of the boundary conditions from the LMDZ simulation around their mean during the 6 h simulation for a given day in October. $\boldsymbol{y}^{\text{bias}}$ is given by the projection of this bias in the observation space through $\mathbf{M}_{\text{integ}}$. Removing the mean ensures reasonable amplitude for the bias. It also

ensures that we do not account twice for errors in the homogeneous background for XCO_2, given that the prior uncertainties in b are already included in the inversion framework.

2.8.3 Monte Carlo sampling of the posterior uncertainties when introducing systematic measurement errors that have a non-Gaussian distribution

In the third set of OSSEs, the systematic measurement errors are introduced in addition to the random measurement noise but model errors from the observation operator are ignored. The spatial variations of the standard deviation of the measurement noise are also accounted for. The distribution of the systematic errors and thus that of the resulting observation errors $\{\boldsymbol{e}_y\}$ is not considered to be Gaussian and it is biased. Such a distribution cannot be perfectly accounted for by the inversion system. The configuration of $\mathbf{R}$ in the inversion system is adapted to fit as much as possible with the distribution of the observation errors given as input to the system. However, in this context, the posterior distribution of errors to the actual control parameters $\{\boldsymbol{e}_s^a\}$ does not follow the $N(\mathbf{0},\mathbf{A})$ distribution. A Monte Carlo framework is thus set up to sample $\{\boldsymbol{e}_s^a\}$ based on the sampling of $\{\boldsymbol{e}_y\}$ and on an ensemble of applications, for each member of the sampling, of

$$\boldsymbol{e}_s^a = \boldsymbol{e}_s^b + \mathbf{K}\left(\boldsymbol{e}_y - \mathbf{M}\boldsymbol{e}_s^b\right). \tag{10}$$

This Eq. (10) is derived by removing the true control parameters in both sides of Eq. (5), and by denoting the prior distribution of errors to the actual control parameters $\{\boldsymbol{e}_s^b\}$.

The corresponding Monte Carlo experiments use only the most realistic spatial sampling of the satellite imagery corresponding to the CarbonSat configuration (SIM-CarbonSat) since they rely on the simulation of random and systematic errors for CarbonSat by Buchwitz et al. (2013). Figure S2 gives an illustration of the systematics errors in the Paris area, which are characterized by patterns of negative or positive errors whose amplitude exceeds 0.1 ppm over 50 to 100 km spatial scales. These simulations of random and systematic errors have also been used by Pillai et al. (2016) to assess the potential of CarbonSat for monitoring city-scale CO_2 emissions. Assessing their level of realism is out of the scope of this study and we refer the reader to Buchwitz et al. (2013) for further details and interpretation.

For a given inversion day, the different simulations of these errors for the different selected passes over the Paris area are used to generate the sampling of measurement errors. This follows the assumption that the statistics of these errors simulated for different days of the year 2010 all follow a single stationary distribution of the measurement error that can apply to any inversion day in October 2010. The OSSEs will thus also have to account for the statistical nature of the cloud cover and of the satellite position. Consequently, each member of the Monte Carlo ensemble has its own structure for $\boldsymbol{y}$ and consistently for $\mathbf{M}$, $\mathbf{R}$ and $\mathbf{K}$ so that the application of Eq. (10) is actually rewritten for the ith member of the ensemble:

$$\boldsymbol{e}_s^a[i] = \boldsymbol{e}_s^b[i] + \mathbf{K}[i]\left(\boldsymbol{e}_y[i] - \mathbf{M}[i]\,\boldsymbol{e}_s^b[i]\right) \tag{11}$$

for $i \in [1\ldots N]$, where $\mathbf{K}[i] = \mathbf{A}[i]\mathbf{M}[i]^{\mathrm{T}}\mathbf{R}[i]^{-1}$ and $\mathbf{A}[i] = \left[\mathbf{B}^{-1} + \mathbf{M}[i]^{\mathrm{T}}\mathbf{R}[i]^{-1}\mathbf{M}[i]\right]^{-1}$.

Errors $\boldsymbol{e}_s^b[i]$ are sampled from the normal distribution $N(\mathbf{0},\mathbf{B})$. The statistics of the actual mean $\boldsymbol{s}_{\mathrm{pract}}^{\mathrm{bias}}$ and covariance $\mathbf{A}_{\mathrm{pract}}$ of the posterior errors $\boldsymbol{e}_s^a[i]$ are computed to characterize the actual uncertainty reduction compared to $\mathbf{B}$. $\boldsymbol{s}_{\mathrm{pract}}^{\mathrm{bias}}$ and $\mathbf{A}_{\mathrm{pract}}$ are called "practical" hereafter, in opposition with the theoretical estimates $\boldsymbol{s}^{\mathrm{bias}}$ and $\mathbf{A}$ from Eqs. (4) and (7).

The derivation of the observation errors $\boldsymbol{e}_y[i]$ and of the corresponding $\mathbf{R}[i]$ matrix is based on the fact that the simulations of random and systematic errors provided by Buchwitz et al. (2013) can be interpreted as maps of the standard deviation $\sigma_y^r[i]$ of the random error $\boldsymbol{e}_y^r[i]$ and values for the systematic errors $\boldsymbol{e}_y^s[i]$. These maps also characterize the structure of $\boldsymbol{y}[i]$. The maps of systematic errors for the 19 passes of CarbonSat over Paris with the highest number of cloud free pixels at less than 100 km from the centre of Paris are given in Fig. S2 in the Supplement. An example of the perturbations of the XCO_2 images with such maps of random and systematic errors is given in Fig. S3. The error $\boldsymbol{e}_y[i]$ for a given ensemble member is thus built using one of such couple of maps for $\sigma_y^r[i]$ and $\boldsymbol{e}_y^s[i]$, as the sum of $\boldsymbol{e}_y^s[i]$ and of a random sample $\boldsymbol{e}_y^r[i]$ of the normal distribution $N(\mathbf{0},\mathrm{diag}(\sigma_y^r[i]^2))$. As generally done for atmospheric inversion, the matrix $\mathbf{R}[i]$ is deliberately built as a diagonal matrix, and thus based on the assumption that there is no temporal or spatial correlation in the observation errors, to ensure that it is easily inverted in Eq. (4). It is derived as the sum of $\mathrm{diag}(\sigma_y^r[i]^2) + (e^s)^2\mathbf{I}_d[i]$, where $\mathbf{I}_d[i]$ is the identity matrix for the $\boldsymbol{y}[i]$ space and e^s is fixed to a typical value for systematic errors equal to 0.3 ppm. This 0.3 ppm value is based on a space and time RMS of the systematic errors over the Paris area in 2010. The addition of the term $(e^s)^2\mathbf{I}_d[i]$ helps the inversion system to anticipate for the systematic errors. However, it cannot perfectly anticipate the structure of these errors due to its inability to account for non-Gaussian and biased errors, and for spatial correlations of the errors. In particular, the complex spatial patterns in the systematic errors, e.g. their correlation to aerosol layers or to the variations in land cover, are a critical issue for the inversion.

In this experimental protocol, the size of the Monte Carlo ensembles is limited by the number of selected maps of measurement errors from Buchwitz et al. (2013), i.e. to $N = 19$ members for each inversion day. The theoretical uncertainty reduction for the 6 h mean emission estimates for each ensemble member given by the comparison between $\mathbf{A}[i]$ and $\mathbf{B}$ is the criteria for the selection of the "19 best observation sampling" used in this ensemble for a given inversion day. The other observation samplings generally have very

few data on the city emission plume (see Sect. 4.2), while we apply the Monte Carlo framework to derive typical scores of uncertainty reduction for cases when the observation sampling can be assumed to be sufficient to support the emissions inversion. This is why we do not increase the size of the Monte Carlo ensemble by including some of these low observation samplings. However, this modest number of ensemble members can raise sampling errors (called hereafter Monte Carlo sampling errors) and the ensembles $\boldsymbol{e}_s^b[i]$ and $\boldsymbol{e}_s^a[i]$ may not fully converge towards $N(\mathbf{0},\mathbf{B})$ and towards the practical statistics of the posterior uncertainty that are looked for.

There is a need to evaluate the impact of these sampling errors and of the realistic simulation of the observation samplings that accounts for cloud cover and for a positioning of the satellite sub-tracks that is not necessarily located over the Paris area. In order to separate it from the impact of systematic errors, an ensemble of inversions is conducted as described above but ignoring systematic errors, i.e. by defining $\boldsymbol{e}_y[i]$ as equal to $\boldsymbol{e}_y^r[i]$ and by deriving the matrix $\mathbf{R}[i]$ as $\mathrm{diag}(\sigma_y^r[i]^2)$. When ignoring the systematic errors, the analysis of the theoretical uncertainty reductions from $\mathbf{B}$ to the set of $\mathbf{A}[i]$, in comparison to those obtained with the more theoretical ("TH") sampling, should illustrate the specific impact of using realistic observation samplings, while the comparison between the set of $\mathbf{A}[i]$ and $\mathbf{A}_{\mathrm{pract}}$ should help characterizing the impact of the Monte Carlo sampling errors. Furthermore, the results from the Monte Carlo experiments are analysed in terms of comparison of the practical posterior uncertainties, $\boldsymbol{s}_{\mathrm{pract}}^{\mathrm{bias}}$ and $\mathbf{A}_{\mathrm{pract}}$, to practical prior uncertainties, $\boldsymbol{s}_{\mathrm{pract}}^{\mathrm{priorbias}}$ and $\mathbf{B}_{\mathrm{pract}}$, which differ from $\mathbf{0}$ and $\mathbf{B}$ due to the Monte Carlo sampling errors.

2.8.4 Monte Carlo sampling of the posterior uncertainties when combining the different types of observation errors

In the fourth set of OSSEs, the observation errors combine the biases in the observation operator and the non-Gaussian and biased distribution of the measurement errors considered in the second and third set of OSSEs. This, again, is only tested for the most realistic spatial sampling of the satellite imagery corresponding to the CarbonSat configuration (SIM-CarbonSat). Accounting for this combination of errors leads to a Monte Carlo ensemble approach solving for, for each ensemble member:

$$\boldsymbol{e}_s^a[i] = \boldsymbol{e}_s^b[i] + \mathbf{K}[i]\left(\boldsymbol{y}^{\mathrm{bias}}[i] + \boldsymbol{e}_y[i] - \mathbf{M}[i]\,\boldsymbol{e}_s^b[i]\right) \quad (12)$$

for $i \in [1\ldots N]$ where

$\mathbf{K}[i] = \mathbf{A}[i]\mathbf{M}[i]^{\mathrm{T}}\mathbf{R}[i]^{-1}$ and

$$\mathbf{A}[i] = \left[\mathbf{B}^{-1} + \mathbf{M}[i]^{\mathrm{T}}\mathbf{R}[i]^{-1}\mathbf{M}[i]\right]^{-1},$$

where all the terms are defined and derived similarly as in Eq. (11) except $\boldsymbol{y}^{\mathrm{bias}}[i]$, which is the resampling of the $\boldsymbol{y}^{\mathrm{bias}}$ term described for the second set of OSSEs on the $\boldsymbol{y}[i]$ structure. Here again, the practical estimates of the posterior uncertainties based on these ensembles need to be compared to the practical prior uncertainties obtained with the corresponding sampling of $N(\mathbf{0},\mathbf{B})$.

2.9 Potential sources of uncertainty that are ignored in the OSSE framework

From the most optimistic set-up to the less optimistic one, the OSSE framework accounts for an increasing number of sources of uncertainty in addition to those directly controlled by the inversion, i.e. the temporal or sectorial distribution of the emissions and their 6 h budget. The measurement errors are fully or partially accounted for in the set-up of $\mathbf{R}$, and fully accounted for in the inputs of the less optimistic inversion experiments. We investigate the impact of uncertainties in the spatial distribution of the emissions, that of uncertainties in the temporal profiles of these emissions within the Paris area and that of uncertainties in the boundary conditions. The impact of uncertainties in the initial conditions is evaluated along with that of the lateral and top boundary conditions using a coarse resolution product, which will miss the fine-scale patterns due to the Paris emissions before the 6 h period of inversion. The fact that the satellite imagery is not sensitive to these emissions is not systematic. Therefore, uncertainties in these emissions could sometimes have some impact when the wind speed is particularly low, but it is expected to be negligible.

However, some major sources of uncertainties are ignored even in the less optimistic case, which prevents consideration of this case as "fully pessimistic". Above all, atmospheric transport modelling errors are ignored, while it can easily generate large uncertainties. If forced with erroneous wind modelling, the simulation of the XCO_2 plume from Paris can have wrong shape and location while the inversion strongly relies on these simulated shape and location to filter the XCO_2 signal associated with the emissions of Paris from the images. Despite the rather smooth variations in space of the NEE, uncertainties in the spatial distribution of the NEE may perturb the results since the inversion relies on the patterns from the assumed distribution to separate it from the Paris emissions. Furthermore, this study uses a simulation of the NEE fluxes for October, when these fluxes are rather weak, which, in principle, should yield better results for the FF emissions than if leading the test in spring or summer when the amplitude of NEE during daytime is much larger. Furthermore, uncertainties in the anthropogenic emissions outside the Paris area but within the model domain could have a critical impact since sources, e.g. in northeastern France can be high and their emission plumes could overlap that of the Paris area. Finally, the impact of the biased and non-Gaussian nature of uncertainties in the fluxes is not assessed. However, it is out of the scope of this study to address such a level of issues.

3 Results with optimistic configurations of the OSSEs

This section presents the results of the inversions when assuming that the theoretical set-up of the inversion system is fully consistent with the actual errors, i.e. the results from experiments "TH" (TH-2, TH-x-ns, THsect-2, THsect-x-ns with $x = 4$, 6, 8 or 10 and ns = 1 or 2) defined by Table 2.

3.1 Some preliminary insights from the model simulation of XCO_2

For each of the 20 inversion days in October 2010, simulations of the XCO_2 field at 11:00 are generated with the observation operator described in Sect. 2.5 and setting $\boldsymbol{\lambda}^b = [1, 1 \ldots 1]^{\mathrm{T}}_{n_\lambda}$ and $b = b^{\mathrm{LMDZ}}$, i.e. by imposing the flux fields and the boundary conditions from Airparif, C-TESSEL and the LMDZ simulation without any rescaling or offset of these products. Figure 1 gives the corresponding image when sampling XCO_2 over the full CHIMERE domain at 2 km resolution for one of the inversion days in October.

The analysis of such images and of the response functions computed as described in Sect. 2.5.4 (Fig. S4) shows that the typical signature of the Paris emissions in the XCO_2 field at 11:00 is a plume whose amplitude is ~ 1 ppm and whose width is ~ 40 km at a distance of ~ 150 km downwind from Paris. This amplitude is similar to the typical measurement random noise assumed for CarbonSat or for the optimistic configuration of the TH-LargeSwath sampling. The spatial gradients of XCO_2 that are generated by either the NEE or the boundary conditions have an amplitude that sometimes reaches the same order of magnitude. Stronger (weaker) wind speeds induce narrower, longer and less intense (wider, shorter and more intense) plumes. For strong wind speeds (above 16 m s^{-1} at 700 m a.g.l.), the CO_2 emitted between 05:00 and 06:00 can reach the domain boundaries before 11:00 and does not systematically have a signature in the domain at 11:00. Wind speeds in October 2010 and at 700 m a.g.l. range quite uniformly between 1 and 17 m s^{-1}, which is representative of the range of wind speeds for the full year.

All these indications imply that the wind should be a critical driver of the performance of the inversion. In the following, the results from the experiments for the 20 different inversion days will thus be presented together as a function of the wind speed. This wind speed is characterized hereafter by its values at 700 m a.g.l. over Paris, assuming that they are well representative of the transport within the mixing layer during the time window of interest. They are averaged in time over the period between the emission time and the CarbonSat overpass time when inverting hourly emissions, or over the hour before the CarbonSat overpass when inverting sectorial emissions.

3.2 Posterior uncertainty when controlling hourly fluxes

Figure 2 displays prior and posterior uncertainties from experiments TH-2 and TH-x-ns when inverting the hourly FF CO_2 emissions and the hourly NEE. This section first focuses on results from TH-2. Figure 2a indicates that, for the satellite configuration close to that of CarbonSat, larger wind speeds lead to smaller uncertainty reduction for the 6 h mean FF emissions. This can be explained by the fact that, with stronger wind, the amplitude of the plume from the city emissions is smaller while the measurement error is independent of the wind speed. Therefore the signal from the emissions is filtered with a smaller signal to noise ratio and thus a higher uncertainty.

However, Fig. 2a also indicates that, while the rule applies for hourly emissions when wind speeds are higher than ~ 6 m s^{-1}, the uncertainty in hourly emissions increases with weaker wind speed for wind speeds that are smaller than ~ 6 m s^{-1}. This is interpreted as the consequence of the overlap between the signatures of consecutive hourly emissions, and thus to the decrease in the potential of the inversion to separate these signatures, when the wind speed is low. This is demonstrated by Fig. 2b, which shows negative correlations between posterior uncertainties in consecutive hourly emissions, whose absolutes values increase when the wind speed decreases. If correlations in the prior uncertainty are all positive or null, which is the case here, negative correlations between posterior uncertainties in control variables arise when the signature of these control variables in the observation space are not perfectly separated by the inversion system. It reflects some aliasing in the corrections from the inversion with an overestimation of some variables balanced by an underestimation of other variables. The combination of larger standard deviations of the posterior uncertainties in control variables with more negative correlations between these posterior uncertainties indicates larger problems of separation. When the wind speed is high, the correlations between posterior uncertainties in hourly emissions are nearly null, potentially due to either/both the weak control of the hourly emissions or/and to the absence of overlapping between the signatures of consecutive emissions despite atmospheric diffusion. However, the uncertainty reduction for the hourly emissions becomes weaker for 0–4 m s^{-1} wind speeds than for 4–7 m s^{-1} wind speeds. Therefore, the decrease in the negative correlations below -0.4 when the wind speed decreases below 4 m s^{-1} is primarily driven by the increasing difficulty of the inversion to separate a given 2 h budget of emissions between the 2 corresponding hours rather than by the increase in the control of the hourly emissions. This issue for solving for the temporal profile of the emissions at the hourly scale does not alter the ability to get a precise estimate for the overall budget of 6 h emissions.

The values obtained for the posterior uncertainty in Fig. 2a are often small compared to the prior uncertainty both for 6 h

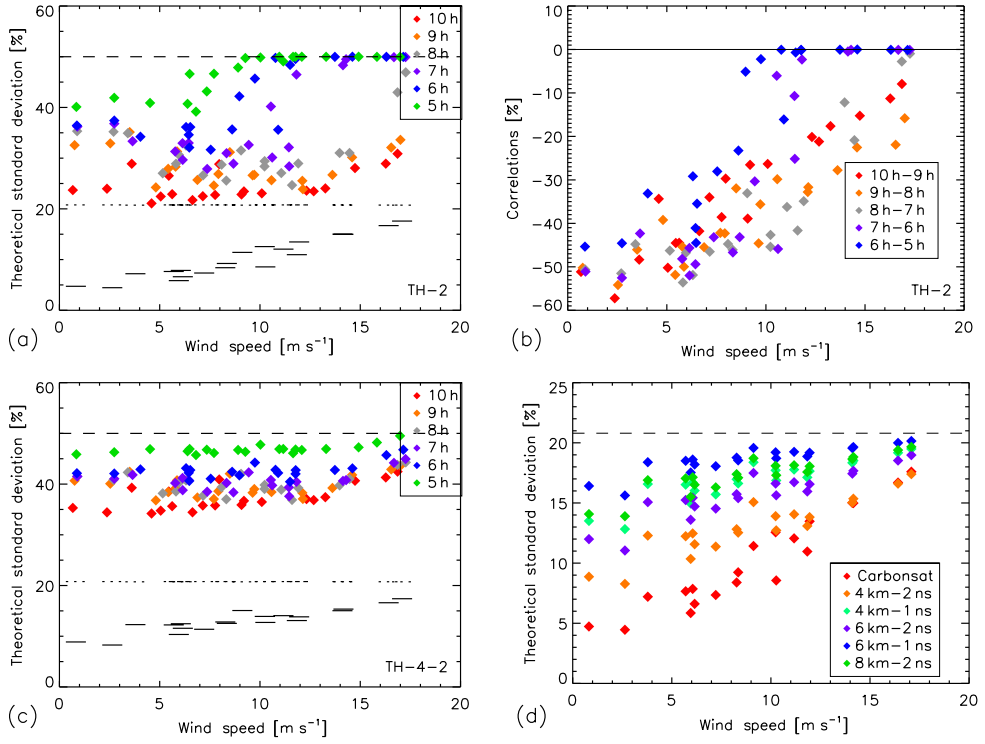

Figure 2. Prior and posterior uncertainties in the FF CO_2 emissions when controlling the hourly fluxes with the optimistic configurations of the OSSEs: results from the 20 inversion days of the TH-2 **(a, b)** and TH-x-ns **(c, d)** experiments given as a function of the average wind speed over Paris at 700 m a.g.l. (over the 6 h duration of the simulation). Prior vs. posterior uncertainties in 1 h mean (dashed black line vs. colour dots) and 6 h mean (dotted black segments vs. full black segments) emissions in TH-2 **(a)** and TH-4-2 **(c)**. Correlations between prior (black lines) or posterior (colour dots) uncertainties in 2 consecutive 1 h mean emissions in TH-2 **(b)**. Prior (black line) and posterior uncertainties (colour dots) in 6 h mean emissions in TH-2, TH-4-2, TH-4-1, TH-6-2, TH-6-1 and TH-8-2 (whose posterior uncertainties are given – in red, orange, light green, purple, blue, and dark green respectively) **(d)**. Uncertainties are given in % of the emission budget given by Airparif. The colours of the dots for a given inversion day are given as a function of the hour of the corresponding 1 h emissions in **(a, b, c)** or as a function of the observation configuration in **(d)**.

mean and hourly emissions. Indeed, for wind speeds smaller than 10 m s^{-1}, the uncertainty reduction is nearly equal to or larger than 50 % for the 6 h mean emissions or for the emissions between 10:00 and 11:00. For wind speeds larger than 10 m s^{-1}, the uncertainty reduction is generally high for the emissions between 10:00 and 11:00 but that for the 6 h mean emissions can be as low as 20 %. The uncertainty reduction for the emissions between 09:00 and 10:00 ranges between 35 and 50 %. It is significantly smaller (between 20 and 50 % for wind speeds smaller than 7–8 m s^{-1}, and less for larger wind speeds) and it has a stronger sensitivity to wind speed for the hourly emissions before 09:00. The signatures of these emissions have been far more diffused through atmospheric transport when observed at 11:00 than that of emissions just before the satellite overpass. This explains these results since atmospheric diffusion decreases the amplitude of these signatures and increases their overlap. It is shown by the values of correlations of the uncertainties in consecutive hourly emissions in Fig. 2b, which are generally more negative for earlier hours. The potential of the system for solving for the temporal profiles before 09:00 is thus rather weak. The uncertainty reduction for the emissions before 07:00 is generally null for wind speeds larger than 11 m s^{-1} due to the signature of the emissions exiting the TH-CarbonSat sampling area.

Hereafter in the text and in the figures, the prior and posterior uncertainties in the fluxes are quantified in a relative way since the inversion system controls scaling factors for the flux estimates in the observation operator, from Airparif and C-TESSEL. For simplification, we will speak about "relative prior and posterior uncertainties", but one should thus keep in mind that these uncertainties are relative to the estimates of the fluxes in the observation operator, not to the prior or posterior estimates of the fluxes. The relative posterior uncertainty in 6 h mean emissions ranges from 5 to 17 % in experiment TH-2. This large spread of the results highlights the critical role played by wind speed in defining the potential of the assimilation of the satellite image for monitoring the Paris emissions.

The correlations between the posterior uncertainties in NEE and $FFCO_2$ emissions are nearly null (not shown). The rather high uncertainty reduction for the Paris FF emissions obtained with experiments TH-2 can thus be partly explained by the good separation between the signature of these emissions and that of the NEE despite the spatial overlapping of these signatures. However, the uncertainty reduction for NEE (not shown) is actually much smaller than for the $FFCO_2$ emissions due to the lower amplitude of their signature (in October). The problem of separating between $FFCO_2$ emissions and NEE may thus be eased by the choice of conducting experiments in October, when the NEE and thus the prior uncertainty in NEE is relatively small. Higher negative correlations between posterior uncertainties in b and $FFCO_2$ emissions (not shown) can be explained by the larger amplitude of prior uncertainties in b than in the NEE. It does not prevent the system from getting a large uncertainty reduction for FF emissions. But a significant part of the posterior uncertainty in FF emissions can be connected to the uncertainties in fluxes outside the model spatial domain or temporal window that are characterized by prior uncertainties in b.

Results when using coarser resolution but wider swath sampling for the XCO_2 observation (experiments TH-x-ns; see the results for TH-4-2 in Fig. 2c) show a behaviour that is similar to that obtained with TH-2. The uncertainty reduction is smaller than for TH-2 except when considering hourly emissions before 08:00, since the signature of these emissions is often visible in the full satellite field of view (FOV) in TH-x-ns, while it is partially or fully outside the satellite spatial sampling in TH-2 (see the comparison between Fig. 2a and d). The skill in decreasing the uncertainty for hourly emissions after 08:00 or for wind speeds smaller than $10\,m\,s^{-1}$ is strongly limited by the observation of XCO_2 at a resolution of 4 km or more with a precision of 1.2 ppm or poorer compared to that when observing XCO_2 at 2 km resolution with a precision of 1.1 ppm. A similar limitation occurs for the reduction of the uncertainty in 6 h mean emissions.

Figure 2d illustrates the dependence of the uncertainty reduction for 6 h mean emissions to the changes in the satellite measurement configuration and mainly to the changes in the spatial resolution and precision of the observation. The relative differences of the scores of uncertainty reduction from experiments TH-x-ns compared to the ones from TH-2 are influenced by the wind speed. In particular, for high wind speeds, the uncertainty reduction is slightly larger for TH-4-2 than for TH-2 since the former gets the signature of the emissions before 08:00. However, for wind speeds smaller than $12\,m\,s^{-1}$, the use of a larger swath for the observation does not impact the mean results significantly, and the uncertainty reduction is approximately decreased by half when dividing the spatial resolution by 2 or when multiplying the measurement noise by 2. Consequently, even if considering results for the lowest wind speeds only, in order to expect a 50 % uncertainty reduction in the 6 h mean emissions, one should not use imagery with a resolution ≥ 6 km and a measurement error close to 2 ppm or poorer.

3.3 Posterior uncertainty when controlling the fluxes per sector and land cover type

The results of the inversions when controlling the budget of the fluxes per sector of anthropogenic activity or per land cover type are detailed below for experiment THsect-2. As when controlling the hourly variations of the emissions (see Sect. 3.2), the results from experiments THsect-x-ns are qualitatively similar but with higher standard deviations of the posterior uncertainties than in THsect-2.

The results for the 6 h mean $FFCO_2$ emissions or NEE are very similar to what was seen when controlling the hourly variations of the emissions (see Sect. 3.2). Accounting for uncertainties in the temporal profiles or in the distribution per type of underlying processes does not modify the ability to get the full budget of the 6 h fluxes. In particular, it does not significantly modify the ability to separate the signature from the $FFCO_2$ emissions and that of the NEE or that of b.

However, the reduction of uncertainty for the individual sectors of emissions shown in Fig. 3a is rather weak. The strong negative correlations between the uncertainties in the different sectors of FF CO_2 emissions in Fig. 3b confirm that the system hardly separates the total budget of the emissions between the different sectors due to the overlapping of their signatures in the XCO_2 field. This is particularly true when considering the highest emissions sectors, i.e. transport and residential combustion. The spatial and temporal distribution of the different sectors of emissions cannot prevent such an overlap since all sectors are distributed all over the Paris urban area.

The uncertainty reductions hardly exceed 25 % for a given sector of emission. The best results are not obtained for the most emitting sector (road transport and residential combustion) but for the sector whose spatial distribution differs the most to that of the other sectors, i.e. industrial combustion. They can reach 50 % for low wind speed, but such a value is not representative of the uncertainty reductions obtained for wind speeds smaller than $10\,m\,s^{-1}$, which rather range between 13 and 30 %.

Overall, these results indicate that, without additional information, the XCO_2 satellite imagery cannot distinguish between the various CO_2 emitting sectors of the Paris area, but that the uncertainty in the sectorial distribution of the emissions does not impact the skill for monitoring the total emissions. Therefore, in the following, we do not analyse the impact of additional sources of uncertainties when controlling this sectorial distribution of the emissions but only when controlling their temporal profile.

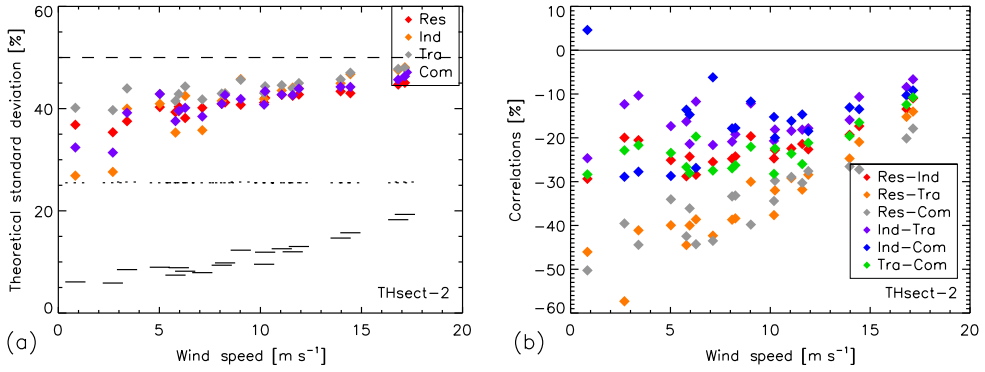

Figure 3. Prior and posterior uncertainties in the FF CO_2 emissions when controlling the fluxes per type of process (Res: residential combustion; Ind: industrial combustion; Tra: transportation; Com: commercial combustion) with the optimistic configurations of the OSSEs: results from the 20 inversion days of the THsect-2 experiment given as a function of the average wind speed over Paris at 700 m a.g.l. (over the 6 h duration of the simulation). Prior vs. posterior uncertainties in sectoral (dashed black line vs. colour dots) and total (dotted black segments vs. full black segments) 6 h budgets of the emissions **(a)**. Correlations between prior (black lines) or posterior (colour dots) uncertainties in the emissions for two different sectors **(b)**. The colours of the dots for a given inversion day are given as a function of the hour of the corresponding 1 h emissions.

4 Results with less optimistic configurations of the OSSEs

4.1 Impact of biases in the observation operator

4.1.1 Biases in the spatial distribution of the Paris emissions

The biases in the posterior estimate of the scaling factors for the emissions of Paris due to the biases in the spatial distribution of the emissions are illustrated for representative cases of the Bdist-2-*r* and Bdist-*x*-ns-*r* set of OSSEs: Bdist-2-15 in Fig. 4a, Bdist-2-45 in Fig. 4c and Bdist-8-2-45 in Fig. 4e. For these cases, the spatial distribution of the emissions is described in the observation operator as a homogeneous distribution in a disc ("15" and "45" referring to the radius of the disc, in km), while the true distribution is assigned to be that of the Airparif inventory. Figure 4b, d and f show the corresponding updates of the posterior uncertainties due to the change of observation operator.

The biases for Bdist-2-15 are negative. They can reach very high negative values: −20 to −40 % for the 6 h mean emissions, below −50 % for the hourly emissions. They are generally below −15 % for both hourly and 6 h mean emissions. The root sum square of such biases and of the random posterior uncertainties shown in Fig. 4b can be considered as the total uncertainties in the emissions. Since the biases are higher in terms of absolute value than the prior uncertainties, they imply an increase rather than a decrease in the total uncertainties from the inversion. These biases are smaller but still very large for high wind speeds.

The biases for Bdist-2-45 are qualitatively and quantitatively very different from that for Bdist-2-15. They are systematically positive for the 6 h mean emissions and positive most of the time for the hourly emissions, but they can also be negative. The amplitude of the biases decreases with higher wind speeds. The values are smaller than for Bdist-2-15 and do not exceed, in terms of absolute values, 15 % for the 6 h mean emissions. They hardly exceed 20 % for the hourly emissions. However, the reduction of the random component of the uncertainty in hourly emissions is generally much lower for Bdist-2-45 than for Bdist-2-15. The scores of uncertainty reduction obtained with TH-2 are between those for Bdist-2-15 and those for Bdist-2-45 and all these experiments show the same qualitative dependency of the results to the wind speed or to the time of the hourly emission considered.

The negative biases with Bdist-2-15 can be explained by the fact that the response functions computed by the inversion system have a smaller extent and a larger amplitude than the "true" emission signatures in this OSSE since the spatial extent of the emissions of Paris in the observation operator is smaller than the actual one. In the extent of the response function of the city emissions modelled with the observation operator, $\left(\mathbf{M}^{\text{true}}_{\text{inventory}} - \mathbf{M}_{\text{inventory}}\right)\boldsymbol{s}^{\text{true}}$ is thus generally negative and it converts into a negative bias in the control vector of the city emissions. A practical interpretation of this is that the system uses only one part of the observed plume of XCO_2 to compute the budget of XCO_2 due to the emissions from Paris, and thus the budget of these emissions, which negatively biases the results. Conversely, in experiment Bdist-2-45, the modelled extent of the Paris emissions is larger and has smaller amplitude than the actual one. The response function to the modelled emissions fully covers the actual plume of XCO_2 from the Paris area. Therefore the inversion system does not miss any portion of the observed XCO_2 plume when computing the budget of XCO_2 due to the emissions from Paris. This explains why

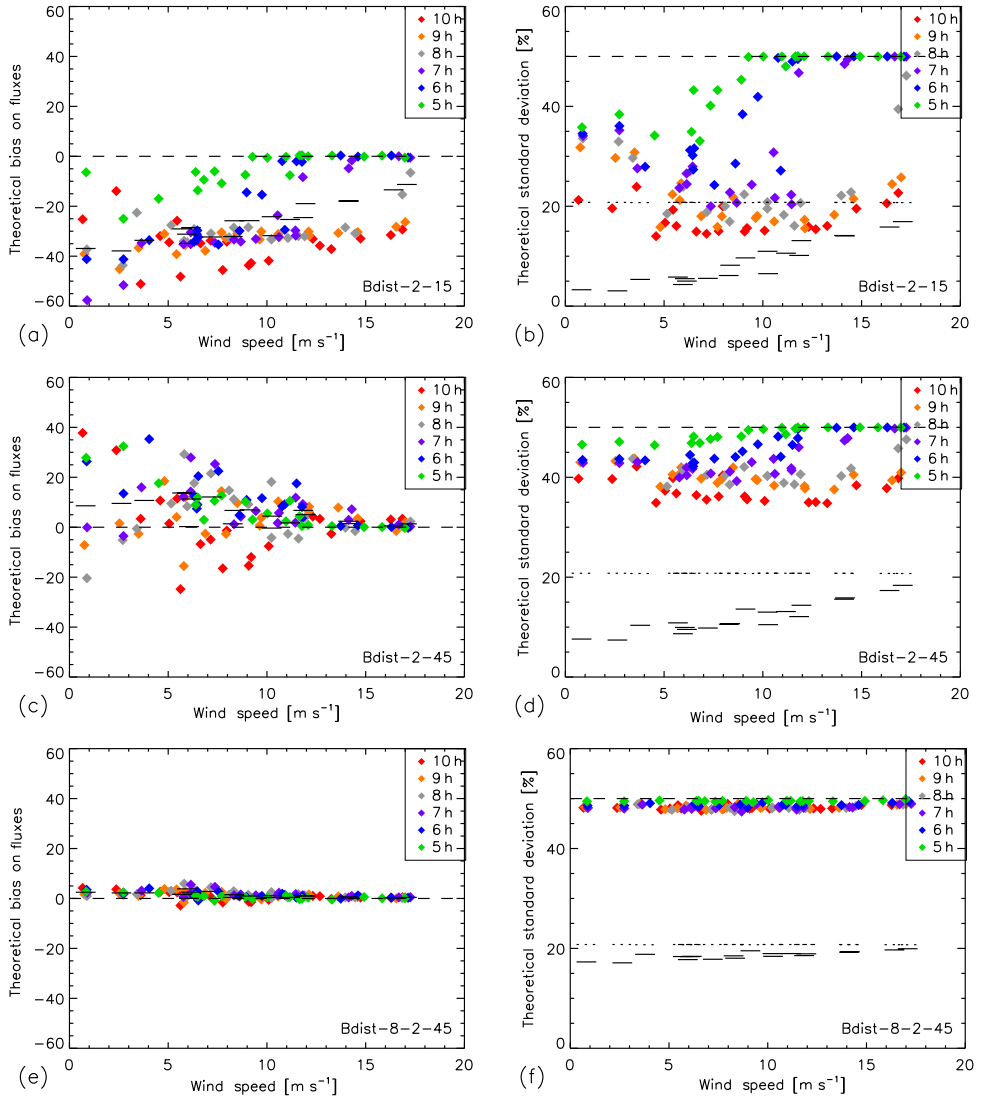

Figure 4. Prior and posterior biases and uncertainties in the FF CO_2 emissions when controlling the hourly fluxes with biases in the spatial distribution of the emissions: results from the 20 inversion days of the Bdist-2-15 **(a–b)**, Bdist-2-45 **(c–d)** and Bdist8-2-45 **(e–f)** experiments given as a function of the average wind speed over Paris at 700 m a.g.l. (over the 6 h duration of the simulation). Prior vs. posterior biases in 1 h mean (dashed black line vs. colour dots) and 6 h mean (dashed black line vs. full black segments) emissions **(a, c, e)**. Prior vs. posterior uncertainties in 1 h mean (dashed black line vs. colour dots) and 6 h mean (dotted black segments vs. full black segments) emissions **(b, d, f)**. The colours of the dots for a given inversion day are given as a function of the hour of the corresponding 1 h emissions.

the resulting bias in the emission budget is relatively small. Still, the term $\left(\mathbf{M}_{\text{inventory}}^{\text{true}} - \mathbf{M}_{\text{inventory}}\right) \boldsymbol{s}^{\text{true}}$ is generally positive within the area of the actual plume and generally negative in the area of the modelled plume that is not covered by the actual plume and the inversion is likely mostly driven by the core of the plume where the NEE signature is, relatively speaking, smaller. This may explain that the bias is positive.

The use of a spatial extent of the emissions that is larger in the observation operator than in the truth implies that the inversion system assimilates more measurement noise in the area covered by the emission response functions and has issues with a larger overlapping of the signatures of the $FFCO_2$ and of the NEE. This explains the higher posterior uncertainties obtained with Bdist-2-45 or TH-2 than with TH-2 or Bdist-2-15 respectively. Assuming a larger area for the $FFCO_2$ emissions in the observation operator also results in having a larger overlapping of the different response functions to hourly emissions, which hampers the uncertainty reduction for hourly emissions. This can explain that the sensitivity to the changes of the spatial distribution of the emissions in the observation operator is weaker for the posterior uncertainty in 6 h mean emissions than for the posterior uncertainty in hourly emissions.

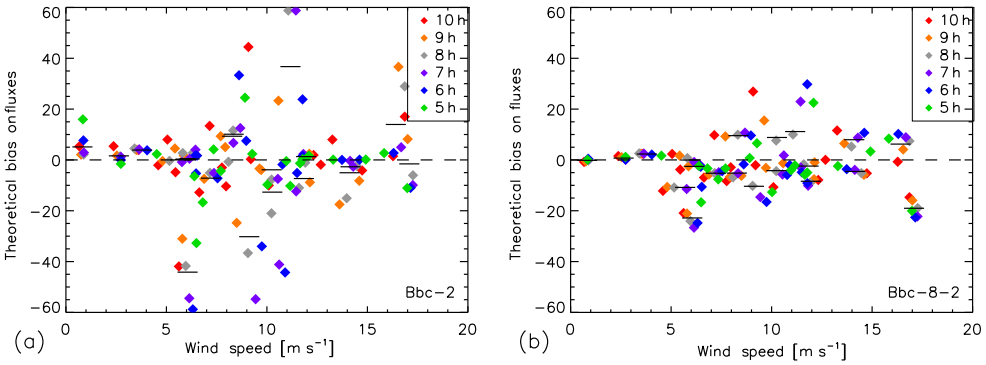

Figure 5. Biases in the FF CO_2 emissions when controlling the hourly fluxes with biases in the boundary conditions: results from the 20 inversion days of the Bbc-2 **(a)** and Bbc-8-2 **(b)** experiments given as a function of the average wind speed over Paris at 700 m a.g.l. (over the 6 h duration of the simulation). Prior vs. posterior biases in 1 h mean (dashed black line vs. colour dots) and 6 h mean (dashed black line vs. full black segments) emissions. The colours of the dots for a given inversion day are given as a function of the hour of the corresponding 1 h emissions.

Consequently, using an upper bound for the extent of the emission distribution when this distribution is poorly known appears to be a conservative decision for the inversion. It avoids taking the risk of missing some parts of the urban area with significant emissions, which would bias the estimates. However, there is therefore a compromise to find between this need to avoid biases and the need for keeping a high uncertainty reduction, which requires not spreading the emissions too much in the observation operator.

The biases obtained with Bdist-8-2-45 (Fig. 4d) are far smaller than those obtained with Bdist-2-45, while, as already analysed in Sect. 3.2, the posterior random uncertainties from Bdist-8-2-45 (Fig. 4e) are much larger than those obtained with Bdist-2-45. This is due to the fact that the corrections applied by the inversion system to the prior estimate of the control parameters when using lower-resolution and noisier imagery (i.e. less and noisier observations) are smaller. This translates into the computation of a "smaller" gain **K**, which yields smaller uncertainty reduction but also a smaller sensitivity to biases in the observation error. Results from other Bdist-x-ns-r experiments follow the behaviour analysed here and in Sect. 3.2 – i.e. they show that larger r, larger x or smaller ns lead to smaller uncertainty reduction but smaller biases.

These results indicate the need for having good knowledge on the spatial extent of the Paris urban emissions before assimilating the satellite imagery, but that knowledge of their distribution within the emitting area need not be precise. This corroborates the results analysed in Sect. 3.3 regarding the weak sensitivity of the inversion to the spatial or sectorial distribution of the emissions within the Paris emitting area. Of note is that this conclusion may be driven by the specificities of Paris in terms of spatial extent and distribution of the emissions.

4.1.2 Biases in the boundary conditions

The biases on the estimates of $FFCO_2$ emissions from Paris due to the biases on the transport model CO_2 boundary conditions that are described in Sect. 2.8.2 are analysed with experiments Bbc-2 (Fig. 5a) and Bbc-x-ns; only the results for experiments Bbc-2 and Bbc-8-2 are shown. The biases in both 6 h mean or hourly emissions can be very high (up to $\pm 60\,\%$) and are generally comprised between $\pm 10\,\%$ for Bbc-2. There is no clear correlation of the biases with the wind speed even though the gain **K** of the inversion is smaller for high wind speeds. The impact of biases in the boundary conditions depends on the spatial structure of their signature in the observation space. The largest biases in the posterior emissions are obtained when the spatial structures of these signatures overlap with the XCO_2 plume from Paris. As when comparing Bdist-x-ns-r experiments to Bdist-2-r experiments in Sect. 4.1.1 and, again, because when using lower-resolution and noisier imagery the corrections and thus the sensitivity to biases in the observation errors are smaller, the biases obtained with Bbc-x-ns experiments are smaller than but highly correlated to that obtained with experiment Bbc-2.

4.2 Impact of the use of a realistic distribution of measurement sampling and errors

The following focuses on the third and fourth sets of OSSEs. They are based on Monte Carlo frameworks using realistic CarbonSat-like samplings of XCO_2 which account for cloud cover and a realistic simulation of the satellite FOV, and using a realistic simulation of both the standard deviation of the measurement noise and of the systematic measurement errors. The MC-2 experiment (Figs. 6, 7a and b) assesses the impact of the limitation of the observation sampling due to cloud cover and instrument FOV, of the Monte Carlo sam-

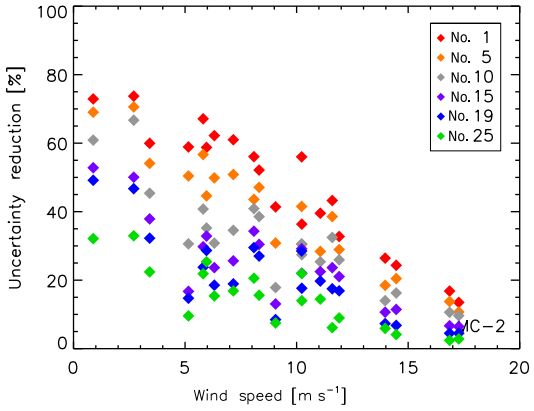

Figure 6. Theoretical uncertainty reduction for the 6 h mean emissions in the MC-2 experiments when using the 1st (red), 5th (orange), 10th (light green), 15th (purple), 19th (blue) and 25th (dark green) best observation sampling provided by the simulation of Buchwitz et al. (2013). The results from the 20 inversion days are given as a function of the average wind speed over Paris at 700 m a.g.l. (over the 6 h duration of the simulation).

pling errors, and, to a lesser extent, of the use of realistic simulations of the measurement noise. Through its comparison to the MC-2 experiment, the MCsyst-2 experiment assesses the impact of the systematic errors (Fig. 7c and d).

Figure 6 shows the theoretical uncertainty reduction for the 6 h mean emissions in MC-2 inversions obtained with the 1st, 5th, 10th, 15th, 19th and 25th best observation sampling provided by the simulation of Buchwitz et al. (2013) for each inversion day (see Sect. 2.8.3). The best observation sampling corresponds to a full coverage of the area within a distance of 100 km from the centre of Paris (Fig. S2) and within an even longer distance in the direction of the emission plume, which depends on the inversion day. This explains why, for a given inversion day, this best observation sampling yields a theoretical uncertainty reduction in experiment MC-2 that is comparable to that of the experiment TH-2 (Fig. 2) with an optimistic sampling of the area over a 150 km distance from the centre of Paris without cloud cover (TH-CarbonSat). Therefore, in a general way, Fig. 6 illustrates the strong impact of the cloud cover and of the limitations associated with realistic instrument FOV through the rapid decline of the theoretical uncertainty reductions between the use of the best observation sampling and that of the following ones. In particular, this figure illustrates the fact that, for the inversion days when the wind speed is above 5 m s^{-1}, the theoretical uncertainty reduction when using the 19th best observation sampling is systematically lower than 30 %. It is even lower than 20 % in most cases. This is generally twice as low as the uncertainty reduction obtained with the 5th to 10th best observation samplings. The uncertainty reduction rapidly decreases to nearly null values when using the 20th and following "best" observation samplings. This reveals that the large majority of the observation samplings simulated throughout the year 2010 brings a weak theoretical constraint on the emission inversions. Even though they do not correspond to the 19 best samplings of any inversion day, the 19 sampling cases of Fig. S2 illustrate how the spatial coverage of the Paris area by the images decreases due to cloud cover and to shifts of the satellite FOV away from the centre of Paris. This figure shows that only 18 samplings provide observations for more than 15 % of the area within a 100 km distance from the centre of Paris. The cloud cover removes 35 to 70 % of the potential data in the satellite field of view near Paris for half of the samplings shown in this figure.

The mathematical framework of the MC-2 and MCsyst-2 experiments is such that, statistically, the limitation of the observation samplings does not bias the practical inversion estimates by itself. However, the Monte Carlo estimations are based on ensembles of 19 members only, which can generate significant Monte Carlo sampling errors. In particular, the mean of these ensembles can be significantly different from zero. The Monte Carlo sampling errors and biases in the posterior ensembles can be influenced by the specific coupling of the different simulations of cloud cover with the different samples of the prior uncertainty and of the measurement noise when building the Monte Carlo ensembles. Figure 7a shows that these biases hardly exceed ±5 % for both the prior and posterior estimates of the 6 h mean emissions. Posterior biases in the 6 h mean emissions are not significantly larger than prior biases even though they bear additional biases from the subsampling in the observation space. However these biases can sometimes exceed ±15 % for posterior estimates of the hourly emissions.

The impact of Monte Carlo sampling errors for the random uncertainty reduction is characterized by the differences, in experiment MC-2, between the practical uncertainty reduction (Fig. 7b) and the theoretical uncertainty reduction for the individual spatial samplings used in this ensemble experiment (Fig. 6). The practical estimates of the uncertainty reduction for 6 h mean fluxes have a negative correlation to the wind speed as the theoretical uncertainty reduction. Ranging from −4 to 70 %, they tend to correspond to the theoretical uncertainty reductions when using the 10th out of 19 best spatial samplings, which range from 10 to 70 %. This indicates that the Monte Carlo sampling error has a limited impact on the practical computation of the random uncertainty reduction. Therefore, the Monte Carlo framework appears to be appropriate for exploring the impact of systematic errors. However, some specific values of the practical uncertainty reduction for the 6 h mean emissions, e.g. 60 % for a wind of ∼ 8 m s^{-1} or the negative value for a wind of ∼ 17 m s^{-1} (Fig. 7b), reveal significant Monte Carlo sampling errors. The impact of the Monte Carlo sampling errors is even more highlighted by the significant number of negative practical uncertainty reductions for hourly emissions (Fig. 7b), while, in theory, given the statistics of errors in experiment MC-2 and the assumption that they are perfectly accounted for by

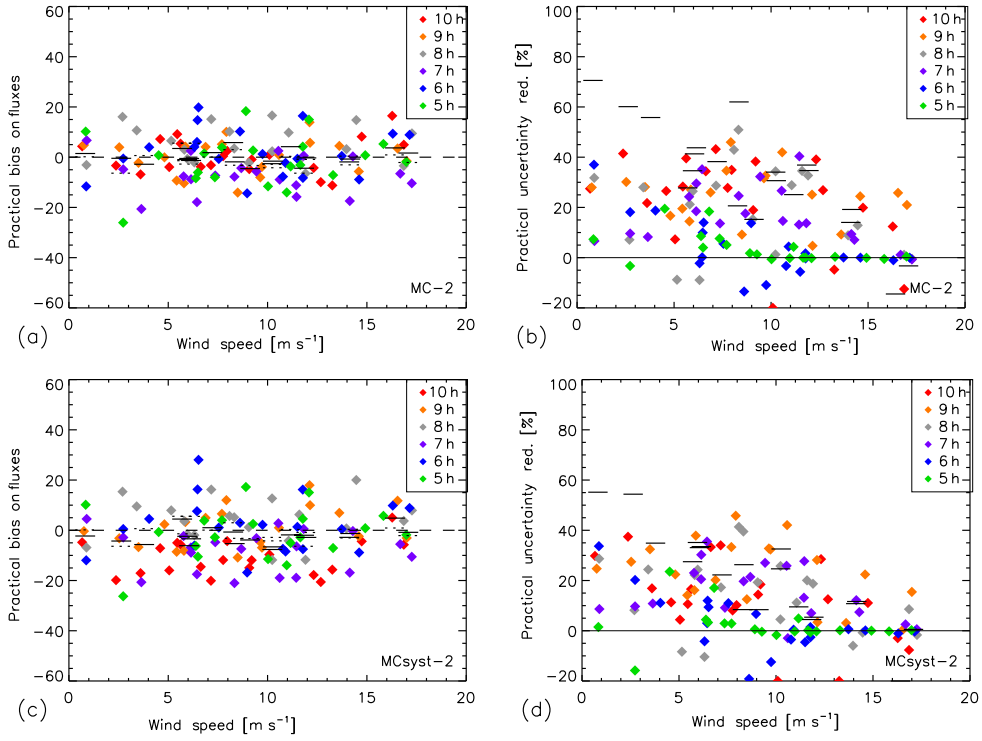

Figure 7. Prior and posterior biases and uncertainty reduction in the FF CO_2 emissions given by the statistics on the Monte Carlo ensembles of inverted emissions in the MC-2 **(a, b)** and MC-syst-2 **(c, d)** experiments with the simulation of the observation sampling and errors (including systematic errors in **c, d**) by Buchwitz et al. (2013). The results from the 20 inversion days are given as a function of the average wind speed over Paris at 700 m a.g.l. (over the 6 h duration of the simulation). Posterior biases in 1 h mean emissions (colour dots) and prior vs posterior biases in 6 h mean emissions (dotted black segments vs. full black segments) **(a, c)**. Practical uncertainty reduction in 1 h mean (colour dots) and 6 h mean (full black segments) emissions **(b, d)**. The colours of the dots for a given inversion day are given as a function of the hour of the corresponding 1 h emissions.

the inversion system, the uncertainty should be decreased by the assimilation of satellite data.

The impact of the systematic errors is given by the direct comparison of Fig. 7c and d to Fig. 7a and b respectively. There is a significant impact of the systematic errors in the posterior biases for both the 6 and 1 h mean emissions (Fig. 7a and c). While posterior biases in 6 h mean emissions ranged quite evenly between ±5 % in MC-2 such as the prior biases, the posterior biases are shifted towards −5 % in MCsyst-2. Similarly, while posterior biases in hourly emissions are generally comprised between ±10 % in MC-2, their spread is larger and shifted to negative values and they often reach 20 % in MCsyst-2. The shift towards negative values can be explained by the fact that the systematic errors as modelled by Buchwitz et al. (2013) are biased negatively in the Paris area. This shift between the practical biases from MC-2 and MCsyst-2 indicates that systematic errors could typically generate 3–4 % biases in the 6 h mean emissions. The biases for the posterior estimates of the emissions between 10:00 and 11:00 in MCsyst-2 are nearly systematically negative, unlike that for other hourly emissions. There is a single positive value, while other values are comprised between −5 and −20 %. This is due to the urban albedo in the Paris area, which generates specific systematic errors over this area, i.e. where the signature of the emissions between 10:00 and 11:00 stand at the time of the satellite overpass.

The uncertainty reductions shown in Fig. 7d are much smaller than those shown in Fig. 7b. The random uncertainty reductions for 6 h mean emissions drop from 55–70 % to ∼ 55 % for low ($< 3\,\mathrm{m\,s^{-1}}$) wind speeds and from 15–60 to 5–35 % for 3 to 15 $\mathrm{m\,s^{-1}}$ wind speeds. The number of negative uncertainty reductions for hourly emissions is not necessarily larger in MCsyst-2 than in MC-2, but the practical uncertainty reductions for hourly emissions are also strongly decreased when accounting for the systematic errors, due to the fact that the distribution of these errors is not Gaussian. The combination between the limited practical random uncertainty reductions and the biases due to systematic errors in experiment MCsyst-2 sometimes implies an increase in the total uncertainties because of the inversion, and in a general way a strong decrease in the total uncertainty reductions compared to results in experiment MC-2.

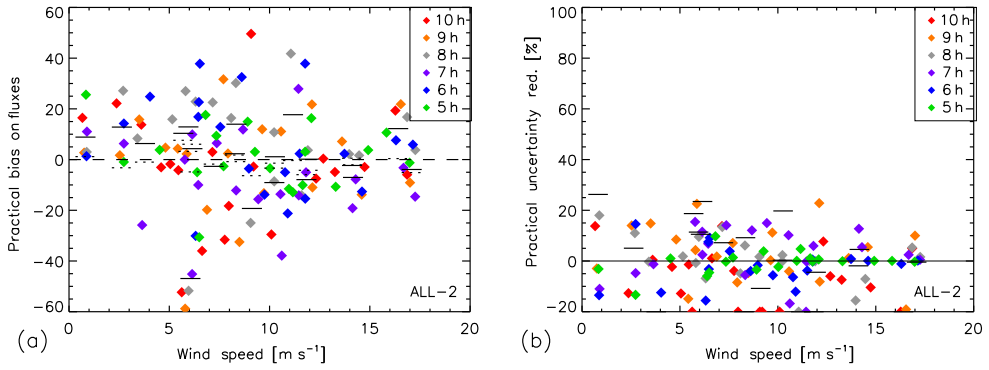

Figure 8. Prior and posterior biases and uncertainty reduction in the FF CO_2 emissions given by the statistics on the Monte Carlo ensembles of inverted emissions in the ALL-2 experiment with the simulation of the observation sampling and errors (including systematic errors) by Buchwitz et al. (2013) and operator biases. Same legends as for the subfigures of Fig. 7.

4.3 Combination of operator biases and of realistic measurement sampling and errors

Figure 8 illustrates the impact of combining the two types of operator biases analysed in Sect. 4.1 and the realistic cloud cover, observation sampling, and random and systematic measurement errors in the Monte Carlo experiment ALL-2. The test is conducted with the use of $\mathbf{M}_{45}^{\mathrm{disc}}$ in the observation operator, while the observations are generated using the distribution of the emissions from Airparif. There is no test using $\mathbf{M}_{15}^{\mathrm{disc}}$ in the observation operator, but the analysis in Sect. 4.1.1 indicates that such a test would lead to a much larger combination of posterior biases and random uncertainties.

Due to the Monte Carlo framework where the cloud cover and satellite FOV vary from one ensemble member to the other one, the impact of biases in the spatial distribution of the emissions or in the model CO_2 boundary conditions of the observation operator is "randomized" in the sense that it varies from one member of the ensemble to the other one. Consequently, adding these biases in ALL-2 compared to MCsyst-2 both increases the biases to very large values in the posterior estimates of the emissions (compare Figs. 8a and 7c) and dramatically degrades the random uncertainty reductions down to large negative values. A part of this decrease should also be attributed to the decrease in the random uncertainty reductions when using $\mathbf{M}_{45}^{\mathrm{disc}}$ instead of the maps from the Airparif inventory in the observation operator (see Sect. 4.1.1), but such a decrease is relatively small compared to that seen between experiments MCsyst-2 and ALL-2. In experiment ALL-2, accounting for the biases and random uncertainties, the total uncertainties in the posterior estimates of the emissions are generally larger than the total prior uncertainties.

5 Discussion and conclusions

This study investigates the potential of satellite XCO_2 spectro-imagery for the atmospheric inversion of the $FFCO_2$ emissions from a megacity. More precisely, it investigates the potential of 2 to 10 km resolution XCO_2 spectro-imagery from sun-synchronous missions based on SWIR absorption measurements. Examples of plans for such missions are the CarbonSat mission, which was a candidate to ESA's Earth Explorer 8 opportunity, and the European mission currently studied by ESA and the European Commission in the context of an increasing political interest for a space-borne monitoring of the CO_2 anthropogenic emissions (Ciais et al., 2015). However, the study also gives some general insights into the potential of SWIR spectro-imagery from other types of CO_2 missions, e.g. the GeoCARB geostationary mission, which has been selected as an Earth Venture Mission by NASA. The study focuses on a relatively easy test case: the monitoring of the emissions from the Paris urban area, whose annual budget is approximately 11–14 MtC yr^{-1}. The assessment of the imagery potential is based on an analytical inversion system and on an OSSE framework developed specifically for this study. This system and this OSSE framework incorporate different levels of assumptions, from the traditional and rather optimistic assumptions underlying atmospheric inversion activities to less idealistic ones. The potential of the imagery is quantified in terms of reduction of uncertainty in the emission estimate, i.e. the relative difference between the uncertainty in the flux prior knowledge exploited by the inversion and that in the inverted (posterior) estimate of the emissions.

An image of the XCO_2 plume from the Paris urban area at a given time does not bear a significant signature of the Paris emissions more than 6 h before. Since the CarbonSat mission was expected to overfly the Paris area in the morning around 11:00 local time, the inversion framework consists in retrieving the emissions between 05:00 and 11:00 based on an image at 11:00 for a given day. The wind conditions influence

the shape and amplitude of the XCO_2 plume from Paris, and thus the imagery potential, which is higher when the emitted CO_2 signal is larger. The inversions are thus conducted for 20 different days of October 2010, which are representative of the range of wind conditions in the Paris area throughout the year, and the sensitivity of the results to the wind speed is analysed.

The realistic simulation of the CarbonSat sampling accounting for cloud cover from Buchwitz et al. (2013) indicates that there should be typically 20 days per year during which the satellite could deliver "appropriate" images that could be used to provide a significant theoretical uncertainty reduction on the emission estimates. Satellites with far larger swath (typically 2000 km for Sentinel-5 instead of ~ 240 km for CarbonSat) and geostationary missions like GeoCARB should provide "appropriate" images at a higher frequency than CarbonSat. Furthermore, the present study does not analyse the potential information brought by the combination of multiple views by the frequent revisit from a given satellite or through the combination of the data from different missions, and it focuses on the potential of individual satellite overpasses. Nevertheless, the low number of "appropriate" acquisitions from CarbonSat within one year indicates that a large fraction of the days during the year are inappropriate to satellite observation of Paris in the SWIR as a result of cloud cover. This, and the fact that the satellite imagery does not bring direct information on the emissions earlier than ~ 6 h before the overpass demonstrates that the satellite SWIR measurement based CO_2 observation alone cannot provide a valid estimate of the daily to annual emissions. In particular, the satellite imagery from a sun-synchronous satellite does not bring direct information on afternoon and night-time emissions if the satellite overpass is around noon. Geostationary SWIR measurements, e.g. with the GeoCARB mission, can fill a large part of this gap in the diurnal cycle of the emissions by potentially providing SWIR data in the morning and in the afternoon and several measurements over a given urban area per day. However, they cannot cover a significant part of the night. Ancillary information such as ground-based measurements, other types of satellite measurements or accurate "bottom-up" knowledge of the temporal profiles from the inventories is required for such a purpose. Obtaining such information for a large number of diverse cities may be challenging. Without ancillary information, the satellite CO_2 spectro-imagery alone may still be useful to monitor trends. This perspective is particularly interesting when the trends of the monitored emissions, i.e. the morning emissions in the case of close-to-noon imagery, are representative of the whole diurnal cycle.

The potential and limitations of different levels of image resolution and precision for monitoring the 6 h emissions before the satellite overpass are investigated with the rather optimistic configuration of the inversions. In this case, the only sources of errors that are accounted for are uncertainties in the 6 h mean budgets of the emissions from Paris and of the NEE in northern France, uncertainties in the hourly or sectorial/per ecosystem distribution of the emissions from Paris and NEE, uncertainties in the XCO_2 background, and satellite measurement noise. Further, the limitation of the observation sampling due to cloud cover or to the fact that the satellite swath is not centred over Paris is ignored. These experiments reveal that one should not use imagery with a resolution ≥ 6 km and a measurement error close to or larger than 2 ppm if targeting a 50 % uncertainty reduction in the 6 h mean emissions from a ~ 22 % relative uncertainty in the prior knowledge on these emissions. When using imagery with a 2 to 4 km resolution and a 1.1 to 1.2 ppm precision, a 5 to 10 % precision on the estimates of the 6 h mean emission can be reached for favourable atmospheric conditions, i.e. when the wind speed in the boundary layer is less than $9\,m\,s^{-1}$. However, the uncertainty reduction would not be better than 25 % if wind speeds were $> 15\,m\,s^{-1}$, even with a 2 km resolution and a 1.1 ppm precision for the measurements. The advantage of using coarser resolution but larger swath imagery for increasing the frequency of revisit over a given city is not investigated in this study, which focuses on the potential of a mission for days when an image is available. Multi-day inversion frameworks would be required to find the best compromise between the resolution and swath of the imagery.

The optimistic experiments also indicate that the imagery could provide information on the temporal profile of the emissions, even though the corresponding estimates of uncertainty reductions for hourly emissions are significantly smaller than those for the 6 h mean emissions. Conversely, the OSSEs indicate a poor ability to solve for the sectorial distribution of the emissions of Paris, and likely their spatial distribution within a known extent. Because of atmospheric diffusion, the differences between the spatial structures of the various sectorial emissions are not large enough to allow for the distinction of their signatures in the XCO_2 images. While the residential and traffic sectors are spread throughout the Paris urban area, the commercial and industrial sectors are more localized, which explains why the uncertainty reduction is slightly higher for these sectors. The lack of ability for monitoring the sectorial distribution of the emission is thus likely strongly related to the specificities of the spatial distribution of the emissions in Paris, which are dominated by diffuse and spatially mixed sources.

Less optimistic experiments are then conducted. They investigate the impact of the uncertainties in the spatial extent of the emissions of Paris, and in the XCO_2 patterns induced by fluxes outside the northern France modelling domain or before 05:00, i.e. by CO_2 initial, lateral and top boundary conditions in the transport model. They also investigate the impact of the limitation of the observation sampling due to cloud cover and to the distance between Paris and the satellite sub-track. Finally, they investigate the impact of the systematic measurement errors due to current uncertainties in the radiative transfer modelling underlying the conversion of

SWIR measurements into XCO_2 data. Biases in the knowledge of the spatial extent of the emissions are shown to be responsible for large negative biases in the inverted emissions if the assumed distribution covers an area smaller than the actual emission area. The Paris urban area is thus not seen as a "point source" whose size would be negligible even if the results from the sectorial inversions indicated that the inversion is weakly sensitive to the distribution of the emissions within the emission area. Spreading the virtual emissions over a large area that necessarily fully covers the actual emission area is a conservative solution for avoiding large negative biases, but it implies smaller uncertainty reductions than when using the proper spatial extension. Biases in the transport model CO_2 boundary conditions that bear the signature of remote fluxes or of fluxes before 05:00 can yield very large biases in the inverted emissions. Finally, when accounting for a realistic observation sampling hampered by cloud cover and systematic errors, the experiments indicate significant biases in the inverted emissions, and moderate random uncertainty reduction compared to the idealistic experiments. The quantitative validity of these last results, derived using a Monte Carlo approach, is limited by the Monte Carlo sampling errors associated with the small ensembles used for the computations. They nevertheless indicate that, for many meteorological and atmospheric conditions, the inversion based on the satellite imagery would hardly improve the prior knowledge on the emissions.

The very last experiments combining all these sources of errors show the worst results, with posterior estimates bearing larger uncertainties than the prior ones. One may argue that these OSSEs use pessimistic assumptions regarding the uncertainties in the spatial distribution of the emissions and in the model boundary conditions. They nevertheless strengthen the conclusion that monitoring the emissions from the Paris urban area with the coupling between state-of-the-art inversion systems and XCO_2 observation capabilities is a difficult challenge. It will be even more difficult for cities with smaller emissions than Paris, which is the case of nearly all cities in Europe, and for cities that have other major cities or large combustion plants in their vicinity. The complementary study by Pillai et al. (2016) assessed the potential of CarbonSat for monitoring the CO_2 emissions of Berlin. The annual emission budget in Berlin is similar to that in Paris, even though Berlin is less populated, since this city bears much larger power plant emissions. Pillai et al. (2016) used the same simulations of CarbonSat data sampling and errors from Buchwitz et al. (2013) as here, but different theoretical frameworks both for the statistical characterization of the errors and the inversions, and different configurations for the modelling and the sources of errors. However, they found results for the mean emissions corresponding to a plume seen during an overpass that are quite similar to those here with 5–20 % random posterior uncertainties depending on the meteorological conditions when ignoring systematic errors in the data and errors in the modelling system, and with high impacts of the systematic errors and of biases in the modelling system.

Based on our results, both the monitoring of the city emissions based on good prior knowledge which is investigated here, and the fully independent verification of an inventory of these emissions using a satellite XCO_2 imagery appear as long-term objectives rather than already mature techniques. This general conclusion is derived based on computations that use both optimistic and pessimistic assumptions. Section 2.9 lists a number of sources of errors that have been ignored in this study, in particular atmospheric transport modelling errors. Present pixel-based inversion techniques strongly rely on the position and extent of the city XCO_2 plume simulated with atmospheric transport models. They assume that transport errors consist in random and unbiased noise with rather simple spatial correlation structures at the image pixel level. In practice, as a consequence of errors in the wind speed and direction, the simulation of the XCO_2 plume position and structure can be poorly related to the actual ones. Large transitory wind direction errors could even lead to situations when the inversion system would not "see" the XCO_2 excess due to the city emissions, in which case the pixel-based assimilation technique would yield quasi-null emission estimates. An inversion procedure that would control simultaneously both transport parameters and CO_2 emissions within a coupled meteorological-CO_2 transport model (Kang et al., 2011) may partially solve these issues. However, due to the complexity of such an approach, it has hardly been investigated in the inverse modelling community, and the result would likely bear significant residual transport errors. The atmospheric transport errors may thus degrade the scores of uncertainty reduction obtained in this study.

Another issue that has been mostly ignored in this study is the strong correlation between the CO_2 and aerosol plumes from the Paris urban area, and thus between the signal that the inversions aim at filtering from the XCO_2 images and a strong source of systematic errors in these images (O'Brien et al., 2016). This could result in high biases in the emission estimates. The simulations of systematic errors by Buchwitz et al. (2013) use a relatively low-resolution aerosol product, which misses the fine-scale patterns of the aerosol plumes from Paris. This explains why we do not attempt at imposing the resulting maps of systematic errors in the Paris area to consistent CO_2 transport conditions, and, in particular, why we use days that are different for the simulation of the systematic errors and for the simulation of the CO_2 transport (see Sect. 2.3).

The NEE during spring and summer that is far larger than in October, and the uncertainties in the anthropogenic emissions outside the Paris area have also been identified in Sect. 2.9 as other sources of errors that would degrade the scores of uncertainty reduction. In particular, during spring and summer, the separation between the signature in the XCO_2 images of the emissions from Paris and of the NEE may not be as good as in October (see Sect. 3.2). Therefore,

a significant part of the large uncertainties in the ecosystem uptake during the growing season could impact the inversion of the emissions from Paris. That and the lower level of emissions during spring and summer than during autumn and winter (due to the decrease in emissions associated with heating) imply that the skills of the inversion could be lower during these seasons.

Conversely, some other components of the experimental framework could be viewed as pessimistic. The way we quantified the impact of uncertainties in the spatial distribution of the emissions and in the transport model CO_2 initial, lateral and top boundary conditions may be seen as extreme (see Sect. 2.8.2). Indeed, it is treated as a bias that is fully ignored by the inversion. The inversion approach generally uses a random representation for all types of errors, including the transport errors due to wrong meteorological forcing, even though it could be improper when these errors relate to processes that seem quite deterministic at the considered timescales. This explains why the cloud cover has been taken as a random parameter of the observation vector in this study. This also explains why systematic errors, which can depend on atmospheric transient properties such as aerosol load, have been considered as random errors. In theory, one could also take this statistical point of view for the errors in the observation operator that have been investigated here, i.e. in the spatial distribution of the emissions and in the boundary conditions. Then, the configuration of the observation error in the inversion system could have been inflated to anticipate for these errors. Still, the complex spatial correlations of the errors from the spatial distribution of the emissions and from the boundary conditions would have hardly been modelled in the inversion system. Therefore, the bias computation in this study can be seen as a qualitative rather than quantitative assessment of the sensitivity to such sources of errors.

It would also seem pessimistic to assume that uncertainties in the emissions spatial distribution could be such that the best knowledge on this distribution would be a homogeneous distribution over a disc. High-resolution satellite imagery of the urban land cover in the visible spectrum from other Earth observation missions should provide at low cost a finer representation of the city, at least in terms of spatial extent, but also regarding the location of power plants, road networks, and industrial, commercial or housing areas. The quantitative impact of uncertainties in the spatial distribution of the emissions could thus be quite smaller than that shown in this study. It does not alter the conclusions regarding the need for a conservative mapping of the emissions in the observation operator over an area that is identical to or larger than the actual area of emissions. A more precise assessment of the impact of uncertainties in the spatial distribution of the emissions was out of the scope of this study. It could rely on the use of relatively independent high-resolution inventories for the city emissions whose difference could be assumed to be representative of the uncertainties in the emissions' spatial distribution (Staufer et al., 2016).

As for most inversion studies, a critical parameter of the experiments that is not objectively defined is the prior uncertainty covariance matrix. Only one configuration of this matrix has been tested in this study with a 50 % uncertainty in the hourly emissions or sectorial budgets of the emissions between 05:00 and 11:00, and, similarly, a 50 % uncertainty in the hourly NEE or in the budgets of NEE per PFT between 05:00 and 11:00. Even though the prior uncertainty in the NEE is relatively high, our results indicate that it does not significantly impact the inversion of the emissions from Paris, and thus that its configuration should not represent a significant issue.

In contrast, the configuration of the prior uncertainty in the emissions could sound rather optimistic for the inversion, since lower prior uncertainties would give lower potential to the inversion for uncertainty reduction and since 50 % is a rather high uncertainty for hourly emissions or for the wide sectors analysed in this study, at least for cities like Paris whose emissions have been regularly inventoried. In general, uncertainties in existing "bottom-up" inventories at city scale are extremely difficult to define, but the order of magnitude for the emissions in cities in Europe should be known approximately even when considering hourly emissions or budgets for the transport, residential, commercial and industrial sectors. However, inventories with temporal variations generally rely on periodical temporal profiles, e.g. with typical diurnal cycles for typical months, so that they can miss strong variations in the actual hourly emissions. Furthermore, such a prior uncertainty could be too low for cities where there is a critical lack of data on fossil fuel consumption, e.g. in developing countries.

The discussion regarding the correlations between prior uncertainties in the different hourly or sectorial emissions is even more difficult, and the resulting ~ 22 to 26 % uncertainties in 6 h mean emissions is debatable. Indeed, if a significant fraction of the uncertainty in the emissions derives from the uncertainty in emissions factors used to build the inventories, a large positive correlation is expected between the uncertainties in the various hourly emission estimates. As indicated above, current inventories provide estimates for average conditions and do not represent transient conditions either related to natural (e.g. cold spell) or human (e.g. holiday, socio-economic events) causes that may apply to several hours in a row. Therefore, large temporal correlations of the uncertainties in hourly emissions or large correlations between uncertainties in sectorial budgets are expected if a significant fraction of these uncertainties are linked to such transient conditions. However, the usual representation of temporal correlations for prior uncertainties in natural fluxes, which uses positive correlations decreasing with increasing time lags, is not well suited to anthropogenic emissions, which have complex cycles at daily, weekly and annual scales and large variability. Note that the existence of

negative correlations between prior uncertainties in hourly or sectorial emissions can also be expected when the hourly and sectorial emissions of the inventories are estimated from the disaggregation of an annual budget. This somewhat justifies that our configuration of the prior uncertainties ignores the correlations between the uncertainties in hourly or sectorial emissions.

Assuming positive correlations would lead to higher uncertainty reductions both because it would increase the prior uncertainty in the 6 h mean emissions and because it would enable extrapolating the information obtained about emissions just before the satellite overpass to earlier emissions. It would also support the assumption that the satellite imagery could bear "indirect" information about the emissions earlier than 6 h before the satellite overpass. From that point of view, the experiments in this study can be seen as pessimistic.

Choosing the Airparif inventory and the CHIMERE transport model as, respectively, the true emissions and transport in the Paris area can bias the diagnostics in this study. Both products are quite diffuse. The Airparif inventory uses typical periodical temporal profiles of the emissions that are homogeneous in space for a given emission sector, and it ignores transient events over short periods of time, which leads to smooth maps, especially for the traffic emissions. The CHIMERE model is an Eulerian model and, as such, is subject to numerical diffusion. This may be viewed as a limitation for separating different hourly or sectorial components of the emissions, and the overestimation of the spread of the emissions in Airparif could yield smaller scores of random uncertainty reduction than if having the actual distribution of the emissions (see Sect. 4.1.1). However, as long as the observation operators in the inversion systems need to rely on such products, any major discrepancies between such products and the actual distribution of the emissions or transport would result in additional sources of errors during the inversion. Furthermore, the Airparif inventory provides the best knowledge on the spatial and temporal distribution of the CO_2 emissions at high resolution within the Paris urban area, and all current inventories that provide temporal variations at the hourly resolution use combinations of typical temporal cycles.

The sensitivity of the inversion to the biases in the transport model CO_2 boundary conditions, the negative correlations between the posterior uncertainties in $FFCO_2$ emissions and in the XCO_2 background b, and the impact of systematic errors demonstrate a rather weak ability of the pixel-based and Gaussian inversion framework to separate the emission plume of Paris from the signatures of other sources or from errors with spatial structures. However, these signatures sometimes seem easy to distinguish from the emission plume of Paris "by eye" (see Fig. S3). It is particularly true when considering the uncertainty in b. Actually, as discussed in this study, the negative correlations in posterior uncertainties, which characterize such a problem of separation, arise as soon as there is some overlapping between the signatures of the different control parameters. Image processing techniques with pattern recognition could help in avoiding such an issue.

Non-Gaussian approaches and inclusion of correlations in the observation errors have already been used in atmospheric inversions, but they generally still rely on simple assumptions. New inversion techniques, potentially based on image data assimilation (Corpetti et al., 2009), could thus help better assimilate XCO_2 images. The combination of XCO_2 measurements with other types of data may critically improve the inversion technique and its potential. There are high uncertainties and temporal variability in the ratios of emission factors between CO_2 and co-emitted species like CO, NO_x, COVs and aerosols. However, the joint assimilation of such co-emitted species and CO_2 data may help constrain the inversion of CO_2 anthropogenic emissions, especially if these data are jointly measured (Rayner et al., 2014). The potential of the spaceborne XCO_2 imagery could also be increased by its integration within an observation system with constellation of satellites, ground-based networks and airborne instruments. A decrease in the systematic errors associated with the retrieval of XCO_2 data from SWIR absorption measurements through an improvement of the inverse radiative transfer models (Buchwitz et al., 2015) would be critical for increasing the potential of the satellite XCO_2 imagery. But in parallel, the improvement of inversion techniques would thus also be needed to increase the potential of such a satellite observation for monitoring the city emissions.

Data availability. The inversion code and CHIMERE simulations corresponding to this study can be provided on request.

The Supplement related to this article is available online at https://doi.org/10.5194/amt-11-681-2018-supplement.

Competing interests. The authors declare that they have no conflict of interest.

Acknowledgements. This study was co-funded by ESA (LOGOFLUX – CarbonSat Earth Explorer 8 Candidate Mission – Inverse Modelling and Mission Performance Study" – ESA contract no. 400010537/12/NL/CO) and by the Chaire industrielle BridGES (a joint research programme between Thalees Alenia Space, Veolia, the Université de Versailles Saint-Quentin-en-Yvelines, the Commissariat à l'Energie Atomique et aux Energies Renouvelables, and the Centre National de la Recherche Scientifique). We would like to thank the Airparif agency, and in particular Olivier Perrussel, for providing the inventory of the CO_2 emissions in the Paris area and expertise on this inventory. We also would like to thank

partners of the LOGOFLUX project (in particular NOVELTIS) and of BridGES for the fruitful discussions we had with them regarding this study.

Edited by: Michel Van Roozendael
Reviewed by: four anonymous referees

References

AIRPARIF: Bilan des émissions de polluants atmospheríques et de gaz à effet de serre en Ile-de-France pour l'année 2010 et historique 2000/2005. Méthodologies et résultats, Tech. rep., AIRPARIF Surveillance de la Qualité de l'Air en Ile-de-France, Paris, France, 2013.

Basu, S., Guerlet, S., Butz, A., Houweling, S., Hasekamp, O., Aben, I., Krummel, P., Steele, P., Langenfelds, R., Torn, M., Biraud, S., Stephens, B., Andrews, A., and Worthy, D.: Global CO_2 fluxes estimated from GOSAT retrievals of total column CO_2, Atmos. Chem. Phys., 13, 8695–8717, https://doi.org/10.5194/acp-13-8695-2013, 2013.

Boussetta, S., Balsamo, G., Beljaars, A., Panareda, A. A., Calvet, J. C., Jacobs, C., van den Hurk, B., Viterbo, P., Lafont, S., Dutra, E., Jarlan, L., Balzarolo, M., Papale, D., and van der Werf, G.: Natural land carbon dioxide exchanges in the ECMWF integrated forecasting system: Implementation and offline validation, J. Geophys. Res.-Atmos., 118, 5923–5946, https://doi.org/10.1002/jgrd.50488, 2013.

Bovensmann, H., Buchwitz, M., Burrows, J. P., Reuter, M., Krings, T., Gerilowski, K., Schneising, O., Heymann, J., Tretner, A., and Erzinger, J.: A remote sensing technique for global monitoring of power plant CO_2 emissions from space and related applications, Atmos. Meas. Tech., 3, 781–811, https://doi.org/10.5194/amt-3-781-2010, 2010.

Bréon, F. M., Broquet, G., Puygrenier, V., Chevallier, F., Xueref-Remy, I., Ramonet, M., Dieudonné, E., Lopez, M., Schmidt, M., Perrussel, O., and Ciais, P.: An attempt at estimating Paris area CO_2 emissions from atmospheric concentration measurements, Atmos. Chem. Phys., 15, 1707–1724, https://doi.org/10.5194/acp-15-1707-2015, 2015.

Buchwitz, M., Reuter, M., Bovensmann, H., Pillai, D., Heymann, J., Schneising, O., Rozanov, V., Krings, T., Burrows, J. P., Boesch, H., Gerbig, C., Meijer, Y., and Löcher, A.: Carbon Monitoring Satellite (CarbonSat): assessment of atmospheric CO_2 and CH_4 retrieval errors by error parameterization, Atmos. Meas. Tech., 6, 3477–3500, https://doi.org/10.5194/amt-6-3477-2013, 2013.

Buchwitz, M., Reuter, M., Schneising, O., Boesch, H., Guerlet, S., Dils, B., Aben, I., Armante, R., Bergamaschi, P., Blumenstock, T., Bovensmann, H., Brunner, D., Buchmann, B., Burrows, J. P., Butz, A., Chedin, A., Chevallier, F., Crevoisier, C. D., Deutscher, N. M., Frankenberg, C., Hase, F., Hasekamp, O. P., Heymann, J., Kaminski, T., Laeng, A., Lichtenberg, G., De Maziere, M., Noel, S., Notholt, J., Orphal, J., Popp, C., Parker, R., Scholze, M., Sussmann, R., Stiller, G. P., Warneke, T., Zehner, C., Bril, A., Crisp, D., Griffith, D. W. T., Kuze, A., O'Dell, C., Oshchepkov, S., Sherlock, V., Suto, H., Wennberg, P., Wunch, D., Yokota, T., and Yoshida, Y.: The Greenhouse Gas Climate Change Initiative (GHG-CCI): Comparison and quality assessment of near-surface-sensitive satellite-derived CO_2 and CH_4 global data sets, Remote Sens. Environ., 162, 344–362, https://doi.org/10.1016/j.rse.2013.04.024, 2015.

Chevallier, F.: On the statistical optimality of CO_2 atmospheric inversions assimilating CO_2 column retrievals, Atmos. Chem. Phys., 15, 11133–11145, https://doi.org/10.5194/acp-15-11133-2015, 2015.

Chevallier, F., Ciais, P., Conway, T. J., Aalto, T., Anderson, B. E., Bousquet, P., Brunke, E. G., Ciattaglia, L., Esaki, Y., Frohlich, M., Gomez, A., Gomez-Pelaez, A. J., Haszpra, L., Krummel, P. B., Langenfelds, R. L., Leuenberger, M., Machida, T., Maignan, F., Matsueda, H., Morgui, J. A., Mukai, H., Nakazawa, T., Peylin, P., Ramonet, M., Rivier, L., Sawa, Y., Schmidt, M., Steele, L. P., Vay, S. A., Vermeulen, A. T., Wofsy, S., and Worthy, D.: CO_2 surface fluxes at grid point scale estimated from a global 21 year reanalysis of atmospheric measurements, J. Geophys. Res.-Atmos., 115, D21307, https://doi.org/10.1029/2010jd013887, 2010.

Chevallier, F., Palmer, P. I., Feng, L., Boesch, H., O'Dell, C. W., and Bousquet, P.: Toward robust and consistent regional CO_2 flux estimates from in situ and spaceborne measurements of atmospheric CO_2, Geophys. Res. Lett., 41, 1065–1070, https://doi.org/10.1002/2013gl058772, 2014.

Chimot, J., Bösch, H., Bovensmann, H., Buchwitz, M., Bréon, F.-M., Camy-Peyret, C., Bacour, C., Van Weele, M., Haan, J., and Veefkind, P.: ESA contract, final report on the study: "Requirements for CO_2 monitoring by Sentinel-5", ESA contract 4000103801, 2012.

Ciais, P., Crisp, D., Denier van der Gon, H., Engelen, R., Janssens-Maenhout, G., Heiman, M., Rayner, P., and Scholze, M.: Towards a european operational monitoring system to monitor fossil CO_2 emissions, Report for the European Commission, 2015.

Corpetti, T., Heas, P., Memin, E., and Papadakis, N.: Pressure image assimilation for atmospheric motion estimation, Tellus A, 61, 160–178, https://doi.org/10.1111/j.1600-0870.2008.00370.x, 2009.

Crisp, D.: Measuring Atmospheric Carbon Dioxide from Space with the Orbiting Carbon Observatory-2 (OCO-2), P. Soc. Photo.-Opt. Ins., 9607, 960702, https://doi.org/10.1117/12.2187291, 2015.

Duren, R. M. and Miller, C. E.: COMMENTARY: Measuring the carbon emissions of megacities, Nat. Clim. Change, 2, 560–562, 2012.

Eldering, A., O'Dell, C. W., Wennberg, P. O., Crisp, D., Gunson, M. R., Viatte, C., Avis, C., Braverman, A., Castano, R., Chang, A., Chapsky, L., Cheng, C., Connor, B., Dang, L., Doran, G., Fisher, B., Frankenberg, C., Fu, D., Granat, R., Hobbs, J., Lee, R. A. M., Mandrake, L., McDuffie, J., Miller, C. E., Myers, V., Natraj, V., O'Brien, D., Osterman, G. B., Oyafuso, F., Payne, V. H., Pollock, H. R., Polonsky, I., Roehl, C. M., Rosenberg, R., Schwandner, F., Smyth, M., Tang, V., Taylor, T. E., To, C., Wunch, D., and Yoshimizu, J.: The Orbiting Carbon Observatory-2: first 18 months of science data products, Atmos. Meas. Tech., 10, 549–563, https://doi.org/10.5194/amt-10-549-2017, 2017.

ESA: Report for mission selection: CarbonSat – An earth explorer to observe greenhouse gases, ESA SP-1339/1 (2 volume series), European Space Agency, Noordwijk, the Netherlands, available at: http://esamultimedia.esa.int/docs/EarthObservation/SP1330-1_CarbonSat.pdf (last access: May 2017), 2015.

Hakkarainen, J., Ialongo, I., and Tamminen, J.: Direct space-based observations of anthropogenic CO_2 emission areas from OCO-2, Geophys. Res. Lett., 43, 11400–11406, https://doi.org/10.1002/2016GL070885, 2016.

Hansen, M. C. and Reed, B.: A comparison of the IGBP DISCover and University of Maryland 1 km global land cover products, Int. J. Remote Sens., 21, 1365–1373, https://doi.org/10.1080/014311600210218, 2000.

Janardanan, R., Maksyutov, S., Oda, T., Saito, M., Kaiser, J., Ganshin, A., Stohl, A., Matsunaga, T., Yoshida, Y., and Yokota, T.: Comparing GOSAT observations of localized CO_2 enhancements by large emitters with inventory-based estimates, Geophys. Res. Lett., 43, 3486–3493, https://doi.org/10.1002/2016GL067843, 2016.

Kang, J. S., Kalnay, E., Liu, J. J., Fung, I., Miyoshi, T., and Ide, K.: "Variable localization" in an ensemble Kalman filter: Application to the carbon cycle data assimilation, J. Geophys. Res.-Atmos., 116, D09110, https://doi.org/10.1029/2010jd014673, 2011.

Kort, E. A., Frankenberg, C., Miller, C. E., and Oda, T.: Space-based observations of megacity carbon dioxide, Geophys. Res. Lett., 39, L17806, https://doi.org/10.1029/2012gl052738, 2012.

Krings, T., Gerilowski, K., Buchwitz, M., Reuter, M., Tretner, A., Erzinger, J., Heinze, D., Pflüger, U., Burrows, J. P., and Bovensmann, H.: MAMAP – a new spectrometer system for column-averaged methane and carbon dioxide observations from aircraft: retrieval algorithm and first inversions for point source emission rates, Atmos. Meas. Tech., 4, 1735–1758, https://doi.org/10.5194/amt-4-1735-2011, 2011.

Krings, T., Neininger, B., Gerilowski, K., Krautwurst, S., Buchwitz, M., Burrows, J. P., Lindemann, C., Ruhtz, T., Schüttemeyer, D., and Bovensmann, H.: Airborne remote sensing and in-situ measurements of atmospheric CO_2 to quantify point source emissions, Atmos. Meas. Tech. Discuss., https://doi.org/10.5194/amt-2016-362, in review, 2016.

Lauvaux, T., Miles, N. L., Richardson, S. J., Deng, A. J., Stauffer, D. R., Davis, K. J., Jacobson, G., Rella, C., Calonder, G. P., and DeCola, P. L.: Urban Emissions of CO_2 from Davos, Switzerland: The First Real-Time Monitoring System Using an Atmospheric Inversion Technique, J. Appl. Meteorol. Clim., 52, 2654–2668, https://doi.org/10.1175/Jamc-D-13-038.1, 2013.

Le Quéré, C., Moriarty, R., Andrew, R. M., Canadell, J. G., Sitch, S., Korsbakken, J. I., Friedlingstein, P., Peters, G. P., Andres, R. J., Boden, T. A., Houghton, R. A., House, J. I., Keeling, R. F., Tans, P., Arneth, A., Bakker, D. C. E., Barbero, L., Bopp, L., Chang, J., Chevallier, F., Chini, L. P., Ciais, P., Fader, M., Feely, R. A., Gkritzalis, T., Harris, I., Hauck, J., Ilyina, T., Jain, A. K., Kato, E., Kitidis, V., Klein Goldewijk, K., Koven, C., Landschützer, P., Lauvset, S. K., Lefèvre, N., Lenton, A., Lima, I. D., Metzl, N., Millero, F., Munro, D. R., Murata, A., Nabel, J. E. M. S., Nakaoka, S., Nojiri, Y., O'Brien, K., Olsen, A., Ono, T., Pérez, F. F., Pfeil, B., Pierrot, D., Poulter, B., Rehder, G., Rödenbeck, C., Saito, S., Schuster, U., Schwinger, J., Séférian, R., Steinhoff, T., Stocker, B. D., Sutton, A. J., Takahashi, T., Tilbrook, B., van der Laan-Luijkx, I. T., van der Werf, G. R., van Heuven, S., Vandemark, D., Viovy, N., Wiltshire, A., Zaehle, S., and Zeng, N.: Global Carbon Budget 2015, Earth Syst. Sci. Data, 7, 349–396, https://doi.org/10.5194/essd-7-349-2015, 2015.

Menut, L., Bessagnet, B., Khvorostyanov, D., Beekmann, M., Blond, N., Colette, A., Coll, I., Curci, G., Foret, G., Hodzic, A., Mailler, S., Meleux, F., Monge, J.-L., Pison, I., Siour, G., Turquety, S., Valari, M., Vautard, R., and Vivanco, M. G.: CHIMERE 2013: a model for regional atmospheric composition modelling, Geosci. Model Dev., 6, 981–1028, https://doi.org/10.5194/gmd-6-981-2013, 2013.

Nassar, R., Hill, T., McLinden, C., Wunch, D., Jones, D., and Crisp, D.: Quantifying CO_2 Emissions From Individual Power Plants From Space, Geophys. Res. Lett., 44, 10045–10053, https://doi.org/10.1002/2017GL074702, 2017.

O'Brien, D. M., Polonsky, I. N., Utembe, S. R., and Rayner, P. J.: Potential of a geostationary geoCARB mission to estimate surface emissions of CO_2, CH_4 and CO in a polluted urban environment: case study Shanghai, Atmos. Meas. Tech., 9, 4633–4654, https://doi.org/10.5194/amt-9-4633-2016, 2016.

Pérez-Landa, G., Ciais, P., Gangoiti, G., Palau, J. L., Carrara, A., Gioli, B., Miglietta, F., Schumacher, M., Millán, M. M., and Sanz, M. J.: Mesoscale circulations over complex terrain in the Valencia coastal region, Spain – Part 2: Modeling CO_2 transport using idealized surface fluxes, Atmos. Chem. Phys., 7, 1851–1868, https://doi.org/10.5194/acp-7-1851-2007, 2007.

Peylin, P., Law, R. M., Gurney, K. R., Chevallier, F., Jacobson, A. R., Maki, T., Niwa, Y., Patra, P. K., Peters, W., Rayner, P. J., Rödenbeck, C., van der Laan-Luijkx, I. T., and Zhang, X.: Global atmospheric carbon budget: results from an ensemble of atmospheric CO_2 inversions, Biogeosciences, 10, 6699–6720, https://doi.org/10.5194/bg-10-6699-2013, 2013.

Pillai, D., Buchwitz, M., Gerbig, C., Koch, T., Reuter, M., Bovensmann, H., Marshall, J., and Burrows, J. P.: Tracking city CO_2 emissions from space using a high-resolution inverse modelling approach: a case study for Berlin, Germany, Atmos. Chem. Phys., 16, 9591–9610, https://doi.org/10.5194/acp-16-9591-2016, 2016.

Rayner, P. J., Utembe, S. R., and Crowell, S.: Constraining regional greenhouse gas emissions using geostationary concentration measurements: a theoretical study, Atmos. Meas. Tech., 7, 3285–3293, https://doi.org/10.5194/amt-7-3285-2014, 2014.

Schwandner, F. M., Gunson, M. R., Miller, C. E., Carn, S. A., Eldering, A., Krings, T., Verhulst, K. R., Schimel, D. S., Nguyen, H. M., Crisp, D., O'Dell, C. W., Osterman, G. B., Iraci, L. T., and Podolske, J. R.: Spaceborne detection of localized carbon dioxide sources, Science, 358, 5782, https://doi.org/10.1126/science.aam5782, 2017.

Sierk, B., Caron, J., Loscher, A., Meijer, Y., Bezy, J. L., Buchwitz, M., and Bovensmann, H.: The CarbonSat candidate mission: Imaging greenhouse gas concentrations from space, P. Soc. Photo.-Opt. Ins., 9218, 92181f, https://doi.org/10.1117/12.2061930, 2014.

Staufer, J., Broquet, G., Bréon, F.-M., Puygrenier, V., Chevallier, F., Xueref-Rémy, I., Dieudonné, E., Lopez, M., Schmidt, M., Ramonet, M., Perrussel, O., Lac, C., Wu, L., and Ciais, P.: The first 1-year-long estimate of the Paris region fossil fuel CO_2 emissions based on atmospheric inversion, Atmos. Chem. Phys., 16, 14703–14726, https://doi.org/10.5194/acp-16-14703-2016, 2016.

Tarantola, A.: Inverse Problem Theory and Methods for Model Parameter Estimation, SIAM, 2005.

Turnbull, J. C., Sweeney, C., Karion, A., Newberger, T., Lehman, S. J., Tans, P. P., Davis, K. J., Lauvaux, T., Miles, N. L., Richardson, S. J., Cambaliza, M. O., Shepson, P. B., Gurney, K., Patarasuk, R., and Razlivanov, I.: Toward quantification and source sector identification of fossil fuel CO_2 emissions from an urban area: Results from the INFLUX experiment, J. Geophys. Res.-Atmos., 120, 292–312, https://doi.org/10.1002/2014jd022555, 2015.

Velazco, V. A., Buchwitz, M., Bovensmann, H., Reuter, M., Schneising, O., Heymann, J., Krings, T., Gerilowski, K., and Burrows, J. P.: Towards space based verification of CO_2 emissions from strong localized sources: fossil fuel power plant emissions as seen by a CarbonSat constellation, Atmos. Meas. Tech., 4, 2809–2822, https://doi.org/10.5194/amt-4-2809-2011, 2011.